JCI insight

Disulfiram inhibits neutrophil extracellular trap formation protecting rodents from acute lung injury and SARS-CoV-2 infection

Jose M. Adrover, … , Robert E. Schwartz, Mikala Egeblad

Research In-Press Preview COVID-19 Immunology

Graphical abstract

Find the latest version:

https://jci.me/157342/pdf

Disulfiram inhibits neutrophil extracellular trap formation protecting rodents from acute lung injury and SARS-CoV-2 infection

Jose M. Adrover[1], Lucia Carrau[2], Juliane Daßler-Plenker[1], Yaron Bram[3], Vasuretha Chandar[3], Sean Houghton[4], David Redmond[4], Joseph R. Merrill[1], Margaret Shevik[1,6,7], Benjamin R tenOever[2,8], Scott Lyons[1], Robert E. Schwartz[3,5,*] and Mikala Egeblad[1,*]

Affiliations:

[1] Cold Spring Harbor Laboratory, Cold Spring Harbor, NY 11724, USA.

[2] Department of Microbiology, Icahn School of Medicine at Mount Sinai. 1468 Madison Ave. New York, NY, 10029, USA.

[3] Division of Gastroenterology and Hepatology, Department of Medicine, Weill Cornell Medicine, 1300 York Ave, New York, NY, 10065, USA.

[4] Division of Regenerative Medicine, Ansary Stem Cell Institute, Weill Cornell Medicine, New York, NY, 10065, USA.

[5] Department of Physiology, Biophysics and Systems Biology, Weill Cornell Medicine, 1300 York Ave, New York, NY, 10065, USA.

[6] Medical Scientist Training Program, School of Medicine, Stony Brook University, Stony Brook, NY 11794, USA

[7] Graduate Program in Pharmacology, Stony Brook University, Stony Brook, NY 11794, USA

[8] Current address: Virology Institute, New York University, Langone Medical Center, New York, NY 10016, USA.

* Correspondence to: Mikala Egeblad, Cold Spring Harbor Laboratory, 1 Bungtown Rd, Cold Spring Harbor, NY 11721, e-mail: egeblad@cshl.edu, phone number (516) 367 6852 or Robert E. Schwartz, Weill Cornell Medicine, 413 East 69th Street, New York, NY 10021, e-mail: res2025@med.cornell.edu, phone number (646) 962 6197

Conflict of interest statement:

Abstract

Severe acute lung injury has few treatment options and a high mortality rate. Upon injury, neutrophils infiltrate the lungs and form neutrophil extracellular traps (NETs), damaging the lungs and driving an exacerbated immune response. Unfortunately, no drug preventing NET formation has completed clinical development. Here, we report that disulfiram —an FDA-approved drug for alcohol use disorder— dramatically reduced NETs, increased survival, improved blood oxygenation, and reduced lung edema in a transfusion-related acute lung injury (TRALI) mouse model. We then tested whether disulfiram could confer protection in the context of SARS-CoV-2 infection, as NETs are elevated in patients with severe COVID-19. In SARS-CoV-2-infected golden hamsters, disulfiram reduced NETs and perivascular fibrosis in the lungs, and downregulated innate immune and complement/coagulation pathways, suggesting that it could be beneficial for COVID-19 patients. In conclusion, an existing FDA-approved drug can block NET formation and improve disease course in two rodent models of lung injury for which treatment options are limited.

INTRODUCTION

Acute respiratory distress syndrome (ARDS) has a high in-hospital mortality rate that increases significantly with age (1). Excessive formation of neutrophil extracellular traps (NETs) is increasingly being recognized as key contributors to acute lung injury (ALI) or ARDS (2–4). NETs are web-like extracellular DNA structures that are formed in response to infection and can ensnare and kill oversized (5) or supernumerary pathogens (6). NETs can also be formed in response to tissue damage or viral infections (7–13). NETs are coated with granule-derived proteins, including proteases and histones that are highly cytotoxic (14, 15). Thus, although NET formation can help contain infections it can also inflict severe damage to the host tissue (4, 14, 16). Indeed, excessive NET formation can directly damage the lung microvasculature (17–20) and promote thrombosis (21–23), leading to multi-organ damage and cardiovascular complications (24). Microvascular damage, thrombosis, and cardiovascular complications are known complications of severe Coronavirus Disease 2019 (COVID-19) (25). Consistently, elevated levels of NETs are found in the blood, thrombi, and lungs of patients with severe COVID-19 (17, 21, 26–28), suggesting that neutrophils and NETs may play an important role after infection with severe acute respiratory syndrome coronavirus 2 (SARS-CoV-2).

Despite the recognized importance of NETs in a variety of diseases (27), including lung injury and cancer, the only FDA-approved NET-targeting drug is the inhaled drug dornase alfa (recombinant DNase I). DNase I can digest NETs present in the airways once they have formed. However, DNase I does not block NET formation or release, and in its inhaled form, it likely has minimal ability to digest NETs beyond the airways. Blocking NET formation by targeting the signaling pathway leading to NET formation is another approach. The enzyme peptidyl arginine deiminase 4 (PAD4) can citrullinate histones, and this modification is required for NETs to form, though NET formation occurring independently of PAD4 has been reported *e.g.*, in response to *Candida albicans* (29). However, while experimental PAD4 inhibitors exist, none has reached clinical trials. The molecule gasdermin

D, which has been proposed to form pores in the nuclear and plasma membranes is important for NET formation (30, 31). Specific gasdermin D inhibitors are in preclinical development, but disulfiram, a drug that has been FDA-approved since 1951, was recently shown to inhibit gasdermin D in macrophages and to increase survival after experimental sepsis in mice (32, 33). Here, we tested the ability of disulfiram to inhibit NET formation and to improve disease outcome in a golden hamster model of COVID-19 and in a classical mouse model of ALI (34): transfusion-related acute lung injury (TRALI). Our data suggest that NETs play an important role in COVID-19 pathogenesis, and that disulfiram, a longstanding FDA-approved drug, can efficiently reduce NET formation and lung injury. These findings have immediate therapeutic implications and highlight the importance of the future development of NET inhibitors.

RESULTS

Disulfiram, an FDA-approved drug, inhibits NET formation

There is a medical need for drugs that can block the formation of NETs. Disulfiram is FDA-approved for the treatment of alcohol use disorder, due to its ability to inhibit aldehyde dehydrogenase (35), but it was recently shown that disulfiram also can block gasdermin D in macrophages (33). Since gasdermin D is important during NET formation, we tested disulfiram's ability to inhibit NET formation ex vivo (**Supplemental Figure 1A**). Disulfiram efficiently blocked phorbol 12-myristate 13-acetate (PMA)-induced NET formation using neutrophils purified from mouse blood (**Figure 1A**) or human peripheral blood (**Figure 1B**), and it blocked NET formation in a dose-dependent manner (**Supplemental Figure 1B**). Disulfiram also greatly reduced NET formation when using RBC-lysed blood instead of purified neutrophils, an experimental condition that reduces neutrophil manipulation and preserves the possibility of interaction with other blood cell types (**Supplemental Figure**

1C). Thus, disulfiram blocks NET formation, likely via its known ability to inhibit gasdermin D polymerization (32, 33).

Disulfiram increases survival in a TRALI model

To test whether disulfiram blocked NET formation in a NET-driven disease model, we used a two-step model of TRALI, in which neutrophils (36, 37), platelets (37, 38), and NETs (3, 4) are known to play prominent roles. In this model, mice are first injected with a low dose of lipopolysaccharide (LPS), and then 24 h later, they are injected with antibodies against major histocompatibility complex (MHC)-I (**Figure 1C**). Within minutes of the antibody injection, severe and acute lung failure develops. Mice subjected to this protocol exhibit acute infiltration of neutrophils to the lung (**Figure 1D** and **Supplemental Figure 1D**); vascular damage leading to the leakage of plasma proteins to the alveolar space (**Figure 1E**); and edema in the lungs (**Figure 1F**). As previously reported (3, 4, 38), we found that neutrophils formed NETs in the lungs of mice subjected to TRALI (**Figure 1G**) and that treatment with the PAD4 inhibitor Cl-amidine (3, 39, 40), which blocks PMA-induced NET formation (**Supplemental Figure 1E**), increased overall survival (**Figure 1H**).

To determine whether disulfiram could inhibit NET formation in vivo in the TRALI model, we treated mice with 50 mg/kg of disulfiram intraperitoneally 24 h and 3 h before injection with antibodies against MHC-I (hereafter termed "TRALI induction", **Figure 2A**). Disulfiram treatment reduced the number of NETs found in the lungs compared to vehicle-treated mice (determined from whole mount tissue cleared lungs, **Figure 2B** and **Supplemental Videos 1** and **2**), without affecting the percentage of neutrophils of all white blood cells or the absolute number of neutrophils in the circulation (**Supplemental Figure 2A-B**). Neutrophil and monocyte infiltration to the lungs were also unaffected by disulfiram treatment (**Supplemental Figure 2C-F**). Importantly, disulfiram treatment caused a dramatic increase in survival: from 40% to 95% (**Figure 2C**, N = 20 mice per group, P = 0.0001). Since gasdermin D blockade in macrophages can reduce interleukin (IL)-1β release (32), we

examined whether disulfiram might in part increase survival in the TRALI model by targeting IL-1ß secretion. However, we found no increase in IL-1β protein levels in the lungs of mice after TRALI induction, regardless of whether mice were treated with disulfiram or not (**Figure 2D**). Furthermore, treatment with anti-IL-1β antibodies (50µg intravenously injected 5 minutes prior to TRALI induction, a dosage reported to block IL-1β in mice [41]) did not increase survival compared to treatment with isotype control antibodies (**Figure 2E**). Hence, the ability of disulfiram to increase survival in the TRALI model correlated with its ability to reduce NET levels in the lung, but not with changes in IL-1β levels.

We next tested other approaches to target NETs in the context of ALI. Inhaled DNase I is FDA-approved and used in cystic fibrosis where NETs accumulate in the alveolar space, increase mucus viscosity, and impair gas exchange [42, 43]. When we administered 200 U of DNase I intranasally, 5 minutes prior to the induction of TRALI, no increase in survival was obtained over vehicle (**Supplemental Figure 2G**). Neutrophil-platelet interactions are important in models of ALI and can induce NET formation [38]. Additionally, NETs and platelets form a forward-feedback loop that can drive the formation of thrombi [23, 44, 45], possibly also in severe COVID-19 [46–49]. However, disruption of neutrophil-platelet interactions [50, 51] by administering the glycoprotein IIb/IIIa inhibitor tirofiban (**Supplemental Figure 2H**) 1 h before TRALI induction or the phosphodiesterase 3 (PDE3) inhibitor dipyridamole (**Supplemental Figure 2I**) 24 h and 3 h before TRALI induction resulted in a small or no survival benefit, respectively. Taken together, these data suggest that systemic inhibition of gasdermin D and NET formation in vivo using disulfiram, an existing FDA-approved drug, shows significant survival benefits in a mouse model of TRALI, as compared to multiple other approaches to target NETs.

Disulfiram improves lung function upon TRALI

After determining that disulfiram blocked NET formation and improved survival of mice upon TRALI induction, we next set out to determine the treatment's effect on lung function. Upon TRALI induction, breathing rate sharply decreased but disulfiram stabilized it compared to the vehicle-treated controls, which continued to experience a further decline in breath rate (**Supplemental Figure 3A**). Disulfiram also resulted in a striking improvement of partial pressure of oxygen after TRALI induction compared to vehicle-treated survivors: a reduction in partial pressure of oxygen was observed during the first 10 min after TRALI induction for both disulfiram- and vehicle-treated mice; however, at the 20 and 40 min time points, the disulfiram-treated mice showed greatly improved oxygenation, whereas the surviving vehicle-treated mice did not show improvement until the 60 min time point (**Figure 3A**). We excluded the non-surviving vehicle-treated mice from this analysis as all the disulfiram-treated mice in the experiment survived, but we note that oxygenation for the non-surviving vehicle-treated mice never improved before they succumbed to the lung injury (**Supplemental Figure 3B**). This data suggest that disulfiram does not protect against the initial lung damage, but prevents the further progression as observed in vehicle-treated animals. Consistent with this idea, we found that although disulfiram significantly reduced the protein content of broncho-alveolar lavage fluid (BALF, **Figure 3B**), the levels were still elevated compared to control mice without TRALI induction. To directly analyze the kinetics of edema formation in disulfiram- and vehicle-treated mice during TRALI, we used longitudinal computed tomography (CT) (**Supplemental Figure 3C**). In these experiments, we found a stark reduction in the volume of edema in the lungs of disulfiram-treated mice compared to their vehicle-treated littermates (**Figure 3C-D, Supplemental Figure 3D** and **Supplemental Video 3**). Taken together, these data suggest that disulfiram treatment did not affect the initial lung damage after TRALI induction, but reduced the progressive vascular damage and edema accumulation, thereby improving oxygenation. It is likely these effects

are responsible for the strikingly increased survival of disulfiram-treated mice upon TRALI induction.

Disulfiram treatment reduces the gene expression of pathways regulating innate immunology and coagulation after SARS-CoV-2 infection in rodents

TRALI is a rare type of lung injury, however, lung injury is a major medical problem in the ongoing COVID-19 pandemic. To test whether disulfiram could be useful in treating COVID-19, we used a golden hamster model (52), and infected hamsters by intranasal injection with 10^3 plaque-forming units (PFUs) of SARS-CoV-2. We evaluated the effects of disulfiram treatment by performing RNA sequencing of lung tissues from SARS-CoV-2-infected hamsters 6 days post infection and treated with disulfiram, starting either 1 day before or 1 day after infection. Disulfiram treatment led to profound alterations in gene expression with more than 1000 differentially expressed genes (P < 0.05, **Figure 4A**, **Supplemental Figure 4A**, and **Supplemental Table 1**). The Gene Ontology (GO) terms showed that the genes with altered expression belonged to several molecular functions and biological pathways (**Figure 4B**, and **Supplemental Table 2**). Among the GO terms regulated upon disulfiram treatment were several related to innate immune function (such as response to IL-1, Pattern Recognition Receptor (PRR) and Toll Like Receptor (TLR) signaling or cytokine signaling) response to oxygen levels, and response to viral life cycle (**Figure 4B** blue, orange and red text, respectively).

We next analyzed the pathways represented by the up- and down-regulated genes after disulfiram treatment. While the pathways of the upregulated genes were not particularly revealing (**Supplemental Figure 4B**), the pathways associated with the genes downregulated by the disulfiram treatment included many related to the innate immune response (**Supplemental Figure 4C** and **Supplemental Table 3**), including TLR cascades and IL-1 signaling. These data suggest that disulfiram treatment may help control an exacerbated innate immune response against SARS-CoV-2. Of note, interferons are key for

antiviral immunity, including against SARS-CoV-2 (53, 54), and we found increased interferon signaling genes and interferon regulatory factors in the disulfiram-treated lungs compared to the vehicle-treated controls (**Supplemental Figure 4D-E**), indicating that interferon responses are not reduced by disulfiram-mediated NET inhibition.

Next, we performed clustering of the Reactome pathways of the up- and down-regulated genes, a method that allows a more in-depth analysis by aggregating biologically-related terms together (55). Interestingly, among the clusters obtained from the disulfiram downregulated genes, we found not only the aforementioned immunity pathways (*i.e.*, in clusters 11, 13, 14, 15, 27 and 34) but also a SARS-CoV infection pathway (cluster 32) **(Figure 4C** [left]**, Supplemental Figure 4F** and **Supplemental Table 4**). These data indicate that at least some members of the infection pathway are downregulated upon disulfiram treatment. Genes that were upregulated in response to disulfiram treatment were associated with several transcriptional pathways (*i.e.*, clusters 9 and 28), nitric oxide production (*e.g.*, cluster 30), metabolic pathways (*e.g.*, clusters 11, 14, or 22), and also P53-related pathways (*e.g.*, cluster 5, 23, or 26, **Figure 4C** [right] and **Supplemental Table 5**).

Finally, when we interrogated the KEGG pathways (**Supplemental Figure 4G**), we found enriched complement and coagulation cascades (cluster 11) in the genes downregulated in the disulfiram-treated group, as well as a cluster including vasopressin-regulated pathways (cluster 10). Activation of both the coagulation cascades and vasopressin is associated with adverse clinical outcomes in COVID-19 patients (49, 56). Among the genes upregulated in disulfiram-treated lungs, we found enrichment of the oxytocin pathways (cluster 11), which has been suggested to be protective against SARS-CoV-2 (57). These data indicate that disulfiram treatment altered the immune response of the SARS-CoV-2-infected lung. Of note, similar functional annotation profiles were achieved regardless of whether the daily disulfiram treatment was started preventatively or 24 hours after infection (see **Tables S6 to S8** for the list of differentially expressed genes, Reactome pathways and GO terms of hamsters treated 24h after infection, and **Supplemental Table 9**

for common GO terms between pre- and post-treatment). Taken together, our RNA-seq data suggest that disulfiram dampens the exacerbated innate immune response after SARS-CoV-2 infection, without impairing natural immunological control of the virus.

Disulfiram reduces NET formation and improves lung histology in SARS-CoV-2-infected golden hamsters

In the TRALI model, disulfiram treatment reduced NET formation, so we next tested whether it had similar effect after SARS-CoV-2 infection in hamsters. SARS-CoV-2 infection induced NET formation in the lungs of the infected hamsters (**Supplemental Figure 5A**), and disulfiram treatment significantly reduced the formation of NETs (**Figure 5A-B** and **Supplemental Videos 4 and 5**). Since comparable reductions in NET formation were observed whether disulfiram treatment started before or after SARS-CoV-2 infection, the two treatment groups were pooled for subsequent analyses. In addition to reduced NET formation, we found reduced neutrophil infiltration in the lungs of the disulfiram-treated hamsters compared to those of vehicle-treated hamsters (**Figure 5C-D**), consistent with the previously reported chemoattractant effects of NETs (23), and our RNAseq data results showing reduced innate immune function. Thus, both the number of neutrophils and the percentage of neutrophils forming NETs were reduced in the lungs after disulfiram treatment, together greatly reducing the total number of NETs. In contrast, the viral load (as determined by the amount of nucleocapsid protein present in the lungs of the infected hamsters) was unaffected by disulfiram treatment (**Figure 5E** and **Supplemental Figure 5B**), indicating that disulfiram treatment does not impair viral clearance. Together with the RNAseq analysis and the analysis of NET formation, this suggests that disulfiram treatment affects the host response to the infection but not the SARS-CoV-2 life cycle or viral clearance.

Golden hamsters do not succumb to SARS-CoV-2 infection, so the response to disulfiram treatment was evaluated at the histological level from hematoxylin & eosin- and

Masson trichrome-stained lung sections. We found that disulfiram treatment was associated with a significant reduction of heavily infiltrated lung area (determined using pixel classifiers that detect hematoxylin-rich areas) (**Figure 5F-G**), and with a trend toward reduced total number of cells (number of cells per total lung area, excluding the alveolar spaces) in the lungs of disulfiram-treated hamsters (**Supplemental Figure 5C-D**). There was also a stark reduction of perivascular fibrosis in the lungs of disulfiram-treated hamsters vs. those of the vehicle-treated hamsters (**Figure 5H-I**). Perivascular fibrosis is associated with increased perivascular edema (58), and consistently, there was a trend towards increased open alveolar space in the lungs of the disulfiram-treated hamsters vs. those of the vehicle-treated hamsters (**Supplemental Figure 5E**). Thus, in golden hamsters infected with SARS-CoV-2, disulfiram treatment reduces NET formation as well as lung inflammation and perivascular fibrosis. This suggests that NET formation contributes to the lung damage during SARS-CoV-2 infection. In contrasts to treatment with disulfiram, treatment with dexamethasone, which has been widely used in the treatment of hospitalized COVID-19 patients (59), did not significantly improve the open alveolar space or in the number of cells per lung area in the SARS-CoV-2 infected hamsters (**Supplemental Figure 5F-H**), but it did significantly decrease perivascular fibrosis (**Supplemental Figure 5I**). Dexamethasone treatment also did not affect the extent of heavily infiltrated lung areas (**Supplemental Figure 5J-K**) or neutrophil infiltration (**Supplemental Figure 5L-M**). Additionally, the viral load was actually increased in the lungs of dexamethasone-treated hamsters, consistent with its ability to dampen immune responses, whereas it was not altered by disulfiram treatment (**Supplemental Figure 5N**). Neither disulfiram nor dexamethasone significantly altered the weight loss observed after SARS-CoV-2 infection (**Supplemental Figure 5O**). Taken together, these data suggest that in SARS-CoV-2 infected golden hamsters, disulfiram treatment confers a benefit and works through a different mechanism of action than dexamethasone.

DISCUSSION

Several diseases have been linked to excessive NET formation, including ARDS and cancer (60). NETs may also play a role in the pathology of severe COVID-19, including as a cause of lung damage and immune thrombosis (21). Here, we show that the blockage of NET formation by the FDA-approved drug disulfiram is associated with dramatically improved survival in a model of TRALI and with improved lung histology in a model of COVID-19. The latter results support the notion that NETs may be one of the drivers of severe COVID-19 pathology, as suggested by us and others (17, 18, 22, 27, 28), although we cannot attribute the effect of disulfiram solely to its ability to block NETs as the treatment caused a global reduction in activation of innate immune signaling pathways. Disulfiram has been used since 1951 and has a well-understood and generally manageable side effect profile (61). Similar to our study on lung injury, a recent report showed a correlation between disulfiram's ability to reduce NET formation and improved survival in a sepsis mouse model (62). Together with our results, this suggest that disulfiram could be useful in the management of pathologies involving NETs, including lung injuries (23, 60, 63, 64), sepsis (62), thrombosis (65), and cancer (66–69). Disulfiram is not compatible with alcohol consumption due to its ability to inhibit aldehyde dehydrogenase (35). Nevertheless, its strong inhibitory effect on NET formation and its improvement of disease outcomes in multiple rodent models highlight the potential for the future development of safe and effective inhibitors of NET formation.

Disulfiram blocked NET formation efficiently in every setting we tested, whether ex vivo or in vivo, and whether targeting human, mouse, or golden hamster neutrophils. Reducing NETs in the mouse TRALI model using DNase I or a PAD4 inhibitor is associated with increased survival, as well as reduced endothelial damage and edema formation (3). Importantly, disulfiram treatment recapitulated these benefits. Disulfiram showed by far the best effects compared to other pharmacological approaches for inhibiting NET formation, including DNase I or PAD4 inhibitors. However, mortality in the TRALI model occurs within minutes which is much faster than in *e.g.*, COVID-19, and we caution that drugs that showed

limited benefit in the TRALI model could still offer protection in other NET-driven diseases. When comparing treatment approaches, we also notice that the administration route of the drugs was different: since DNase I is only available for human use in inhaled form, we administered it via the intranasal route. However, although DNase I can improve symptom management in cystic fibrosis where NETs are found in the alveolar space (42, 43), inhaled DNase I had limited effect on survival in the TRALI model, where intravascular NETs have been reported (3). Thus, we caution that the intranasal route may not deliver sufficient levels of drugs to the location where NETs need to be targeted during ALI. A separate issue is that DNase I targets NETs that have already formed and been released, while disulfiram and PAD4 inhibitors prevent the formation of NETs *ab initio*. DNase I degradation of the DNA backbone of NETs has been reported to leave several other components of NETs *in situ*, including proteases and histones (70), and these may be detrimental in certain contexts (71). It is also unclear whether the release of NET-entrapped cytotoxic compounds into the bloodstream would have a detrimental effect elsewhere. Hence, drugs that block NET formation and those that digest them may affect disease progression differently and may also have different side effects.

An interesting difference between the TRALI and SARS-CoV-2 models was that disulfiram reduced neutrophil infiltration in the latter but not the former model. NETs expose cytoplasmic material and can increase neutrophil infiltration through a variety of mechanisms (72). We speculate that during the short time span of the TRALI model (2 hours), there is not enough time to observe a NET-driven, secondary neutrophil infiltration. Additionally, disulfiram does not appear to inhibit the primary infiltration of neutrophils observed after injection of anti-MHC I antibodies. In contrast, In the SARS-CoV-2 model, the disease develops over the course of several days, allowing sufficient time for NETs drive secondary neutrophil infiltration, an effect that disulfiram would be able to block by preventing NET formation. We therefore interpret the difference in the effects of disulfiram on neutrophil infiltration to derive, at least partially, from the ability of disulfiram to reduce neutrophil

infiltration secondary to NET release, an effect that would only be observed in the SARS-CoV-2 model.

The effect of disulfiram treatment on the survival of mice experiencing TRALI was very dramatic and correlated with reduced NET formation in the lungs, consistent with the hypothesis that it acts by blocking gasdermin D in neutrophils. Gasdermin D is also required for pyroptosis and is involved in IL-1β secretion [73], and disulfiram has been shown to block these processes [32]. In the TRALI model, our data suggest that IL-1β plays a minimal role, as a) IL-1β levels in the lungs were not increased upon TRALI induction, and b) treatment with IL-1β blocking antibodies did not increase survival. Nevertheless, increased IL-1β secretion likely contributes to COVID-19 [74], though blocking antibodies did not reduce mortality in clinical trials of severe COVID-19 [75]. While we focused on the effect of disulfiram in NET-formation, we cannot exclude that disulfiram may also improve disease outcome by affecting other processes, such as pyroptosis and IL-1β release, especially in the SARS-CoV-2 infection model. Experimentally untangling the effects of blocking gasdermin D in neutrophils versus e.g., macrophages, would require the availability of conditional knock-out models. We did observe that the IL-1β pathway was enriched among the significantly downregulated genes upon disulfiram-treatment on SARS-CoV-2-infected hamsters, which would be consistent with inhibition of gasdermin D also in macrophages. Thus, it is possible that disulfiram could benefit patients by reducing both IL-1β secretion and NET formation. Of note, disulfiram appeared in a high-throughput screening for drugs able to inhibit M^{pro}, a SARS-CoV-2 protease, hinting that in the context of COVID-19, disulfiram may confer protection beyond host effects [76].

The RNA-seq analysis showed that many genes downregulated by disulfiram belonged to pathways related to the innate immune response. This result suggests either that disulfiram has broad effects on innate immune cell activities, that formation of NETs in the SARS-CoV-2-infected lungs contributes to further innate immune activation or, perhaps

most likely, a combination of both. Disulfiram treatment also reduced perivascular fibrosis, which would be consistent with reduced perivascular invasion by immune cells and a reduction in associated perivascular edema formation (77), effects we could not formally measure due to restrictions on experiments involving live SARS-CoV-2. Perivascular fibrosis can lead to increased flow resistance and subsequent pulmonary hypertension, which has been described in patients with severe COVID-19 (78). Perivascular fibrosis is also critical in the context of myocardial damage (79), and gasdermin D inhibition has recently been shown to be protective in acute myocardial infarction (80), so it is possible disulfiram could also ameliorate the cardiovascular symptoms of COVID-19 (46). Disulfiram treatment reduced gene expression of coagulation-related pathways, and it is worth noting that NETs are well known to activate the coagulation cascade and promote thrombi formation (23), and that COVID-19 related coagulopathy is one of the key drivers of mortality (49). Finally, dexamethasone, which is widely used for COVID-19 treatment, appeared to confer less of a benefit on lung pathology in SARS-CoV-2-infected hamsters than disulfiram under our experimental conditions. At the same time, dexamethasone, but not disulfiram, significantly increased the viral load in the lungs when administered from day 1 post-infection, consistent with previous reports on the effects of corticoid therapies on respiratory viruses (81). These data support that disulfiram could have utility in the treatment of SARS-CoV-2 infected patients.

Taken together, our data support the notion that disulfiram-mediated blockade of NET formation could be effective at taming the exacerbated immune activation and immunothrombosis seen in severe COVID-19 patients. Additionally, observational studies have suggested a benefit of disulfiram treatment in COVID-19 (82, 83), and clinical trials in the outpatient and inpatient settings are ongoing or recently completed (NCT04485130 and NCT04594343). Finally, although disulfiram is not specifically a NET inhibitor, its ability to block NETs may be worth exploring beyond COVID-19.

MATERIALS AND METHODS

Study design

The objective of this study was to test the hypothesis that disulfiram can block NET formation and reduce lung injury, including in animal models of TRALI and COVID-19. Sample sizes and endpoints for both the TRALI and COVID-19 models were pre-determined by our previous experience with these models. We did not use any data exclusion methods, and no data was excluded. No randomization or blinding methods were used in this study.

Mice

All experiments were performed in 7- to 12-week-old, male BALB/c mice (BALB/cAnNCrl) purchased from Charles River Laboratories, housed in a non-barrier animal facility at Cold Spring Harbor Laboratory (CSHL) under a 12 h light/12 h dark schedule, with water and chow available *ad libitum*. Mice were acclimatized to the animal housing facility for one week prior to performing experiments. All experiments with mice were conducted in accordance with procedures approved by the Institutional Animal Care and Use Committee (IACUC) at CSHL and the National Institutes of Health (NIH) Guide for the Care and Use of Laboratory Animals.

Flow cytometry and cell sorting

Flow cytometric analyses were performed using a Fortessa Analyzer (BD Biosciences). Analysis was performed using FlowJo v10 (Tree Star Inc, Ashland, OR, USA). Cell sorting experiments were performed using an FACS Aria cell sorter (BD Biosciences, USA). All analyses were conducted at the Flow Cytometry Core Facility at CSHL. The following antibodies were used in this study:

- **CD11b-PE**, clone M1/70, Tonbo biosciences (50-0112-U100)

- **Ly6G-AF647**, clone 1A8, Biolegend (127610)

- **CD45-APC/Cy7**, clone 104, Biolegend (103116)

Absolute quantification was done using Trucount absolute counting beads (BD Biosciences, #340334) according to the manufacturer's instructions.

Isolation of blood neutrophils for ex vivo NET formation assays was performed by fluorescence activated cell sorting (FACS), as described (84). Briefly, blood was drawn into EDTA-coated tubes, red blood cells (RBCs) were lysed in ACK (Ammonium-Chloride-Potassium, Gibco, USA, #A1049201) lysis buffer (Thermo Fisher, USA), and blood cells were stained with antibodies against Ly6G (BioLegend, USA). Immediately prior to flow cytometric analysis, DAPI was added to the cells so that only viable (DAPI-), Ly6G+ cells were collected.

Analysis of lung samples by flow cytometry were conducted as previously reported (84). Briefly, the lungs were extracted, placed in cold PBS and processed immediately after. They were digested in HBSS with liberase (1U/ml, Roche) and DNAse I (1 mU/ml, Sigma) for 30 min at 37°C. Single-cell suspensions were incubated with antibodies against CD45, CD11b and Ly6G. Immediately prior to flow cytometric analysis, DAPI was added to the suspension.

Ex vivo NET formation assays with mouse neutrophils

Neutrophils were sorted as described above and 4×10^4 neutrophils were plated in serum-free RPMI medium on poly-L-lysine covered 8-well µ-Slides (Ibidi, Martinsried, Germany), and left for 30 min at 37°C in a cell culture incubator to adhere. Cells were plated in a drop of medium in the center of the well to enhance their adhesion in the central area of the well and to avoid their deposition in the edges. In experiments using RBC-lysed blood, the red blood cells were lysed in ACK buffer, the remaining cells were centrifuged (500 x g at 4°C), the

supernatant was discarded, and the pellet was resuspended directly in RPMI medium. The volume equivalent to 75 μl of the original blood was plated per well, again on poly-L-lysine covered 8-well μ-Slides as a centered drop and left 30 minutes to adhere as described above. For both sorted neutrophils and red blood cell-lysed blood, cells were subsequently incubated for 2h with 100nM Phorbol 12-myristate 13-acetate (PMA) or vehicle, or PMA together with test compound (at the concentrations indicated in the relevant Figure legends). Cells were then fixed using 4% paraformaldehyde (PFA) in phosphate-buffered saline (PBS) for 10 minutes, blocked and permeabilized with PBS containing 0.1% Triton X-100, 25% Fetal Bovine Serum (FBS) and 5% Bovine Serum Albumin (BSA), and stained with antibodies against citrullinated histone 3 (citH3, ab5103 from Abcam, Cambridge, UK) and myeloperoxidase (MPO, AF3667 from R&D Systems, USA) in 1:200 dilution in blocking buffer, at 4ºC overnight. Then, the cells were washed and stained with secondary antibodies: donkey-anti-goat-AF647 (#A21447, Invitrogen, USA) and donkey-anti-rabbit-AF568 (#A10042, Invitrogen) 1:400 and counterstained with DAPI (1:1000) for 2h at room temperature. Z-stack images were acquired with a SP8 Microscope (Leica, Germany) analyzed using Imaris (Bitplane) or using custom-made ImageJ macros (see "*Code availability*" section) to identify NETs (defined as triple-positive co-localization events of DNA, citH3, and MPO).

Antibody-induced acute lung injury (ALI)

A two-event model of transfusion-related ALI (TRALI) was adopted for our studies, essentially conducted as described (37). Male BALB/c mice from Charles River (7 to 12 weeks old) were injected intraperitoneally with 0.1 mg/kg lipopolysaccharide (LPS) from *Escherichia coli* (O111:B4, Sigma, USA). Twenty-four hours later, TRALI was induced by intravenously injecting mice with 1 mg/kg anti-H2d (clone 34-1-2s; BioXcell) antibody. Some mice were treated 1h before injection of the anti-H2d antibodies (TRALI induction) with 12mg/kg of Cl-amidine injected intravenously (Cayman Chemical Company, Ann Arbor,

Michigan, USA) to block NET formation. Other groups were treated with 200 U of intranasally injected DNase I (DNase I recombinant, Roche, Switzerland) in PBS, 5 minutes before TRALI induction; 0.1mg/kg tirofiban (tirofiban hydrochloride monohydrate, Sigma) intravenously injected 1 h before TRALI induction; 8mg/kg dipyridamole intraperitoneally injected 24 h and 3 h before TRALI induction; 50μg of anti-IL-1β (InVivoMAb anti-mouse/rat IL-1β, clone B112, BioXCell) or isotype control (InVivoMAb polyclonal Armenian hamster IgG, BioXCell) intravenously injected 5 minutes before TRALI induction; or 50mg/kg intraperitoneally injection of disulfiram (tetraethylthiuram disulfide from Sigma) in sesame oil 24 h and 3 h before TRALI induction. For survival experiments, mice were observed for 2h after TRALI-induction (the acute phase of ALI). In some experiments, pO$_2$ (%) was measured using a MouseOx Pulse Oximeter (STARR Life Siences Corp, USA), approximately every 10 minutes after injection of the anti-H2d antibodies.

Whole mount immunostaining and tissue clearing

To determine the abundance of NETs in the lungs of mice after TRALI induction, we performed whole mount immunostaining and tissue clearing of excised lungs as previously described (3). For these experiments, mice were euthanized with CO$_2$ 40 min after TRALI induction. Mice were then perfused with 20mL of saline through the left ventricle of the heart, and the lungs were collected in cold PBS. Afterwards, lungs were fixed at 4°C overnight in PBS with 4% PFA and 30% sucrose. After three washes with PBS for 1 h each at room temperature, tissues were permeabilized in methanol (MetOH) gradients in PBS (PBS > MetOH 50% > MetOH 80% > MetOH 100%, for 30 min in each solution). Then, tissues were bleached with Dent's bleach (15% H$_2$O$_2$, 16.7% Dimethyl sulfoxide [DMSO] in MetOH) for 1h at room temperature and rehydrated through descending methanol gradients in PBS (MetOH 80% > MetOH 50% > PBS, 30 min in each solution). Then tissues were incubated with blocking buffer containing PBS with 0.3% Triton X100, 0.2% BSA, 5% DMSO, 0.1% azide

and 25% FBS overnight at 4ºC with shaking. Afterwards, lungs were stained with antibodies against citrullinated histone 3 (rabbit, Anti-Histone H3-citrulline R2 + R8 + R17 antibody, Abcam), MPO (goat, Human/Mouse Myeloperoxidase/MPO Antibody, R&D Systems) and CD31 (Purified Rat Anti-Mouse CD31, Clone MEC 13.3, BD), all 1:200 in blocking buffer for 2 days at 4ºC with shaking. After washing for 24 h in washing buffer (PBS with 0.2% Triton X100 and 3% NaCl), the tissues were stained with secondary antibodies donkey-anti-rabbit-AF568 (A10042, Invitrogen, USA), donkey-anti-Rat-AF488 (A212008, Invitrogen) and donkey-anti-goat AF647 (A21447, Invitrogen) 1:400 for 24 h at 4ºC with shaking. Twenty-four hours later, tissues were washed for 24 h in washing buffer and thereafter dehydrated in MetOH gradients in dH_2O using glass containers (MetOH 50% > MetOH 70% > MetOH 90% > 3x MetOH 100%, 30 min for each step). Then, tissues were cleared for 30 min in 50% MetOH and 50% benzyl alcohol, benzyl benzoate (BABB, mixed 1:2) and 1 h in 100% BABB, and finally, imaged on an SP8 Microscope (Leica, typical Z-depths of 200-500µm). Quantification was performed with Imaris software (Bitplane), using spots on a triple-colocalization channel of DNA, MPO, and citrullinated histone 3. Neutrophils were quantified using spots based on MPO signal. Frequency was calculated as the number of NETs / number of neutrophils in the 3D volume.

Mouse tissue section immunostaining
4% PFA-fixed and optimal cutting temperature (OCT)-embedded tissues were cut in 5µm sections, incubated for 1h at room temperature in blocking buffer (PBS containing 10% BSA and 2% goat serum) and stained for 1h at room temperature with 1:200 rabbit anti-mouse laminin (Sigma) in blocking buffer diluted 1:2 in PBS. Tissues were then washed, and further stained for 1h at room temperature with Dylight650-labeled anti-Ly-6G (clone 1A8; BioXcell, USA) and phycoerythin-labeled anti-CD41 (eBiosciences, USA) at 1:200, and AlexaFluor 488 Goat anti-rabbit IgG (Molecular Probes) diluted 1:500 in blocking buffer. Finally, samples

were counterstained with DAPI (Sigma) and mounted with Mowiol medium. Images were captured on a Leica SP8 microscope.

Computed tomography (CT) for lung edema quantification

Mice were anesthetized with 150 mg/kg ketamine and 10 mg/kg xylazine. Once anesthetized, mice were positioned prone on the imaging cradle and secured with tape and gauze to minimize motion. After a 2D scout scan, a baseline x-ray CT scan covering the lungs and airways was acquired with the CT component of a Mediso nanoScan PET/CT system (Mediso USA, Arlington, VA, USA). The x-ray parameters were a beam energy of 50kVp and exposure of 183µAs, in an axial scan with 1080 projections. Total scan time was 7 minutes. Images were reconstructed in Nucline software version 3.00.020 (Mediso USA) to a voxel size of 138µm isotropic using a Butterworth filter at 100% cutoff. After the baseline scan, the cradle was moved out of the imaging bore so that antibodies against MHC-I (see "*Antibody-induced acute lung injury*" section) could be injected retro-orbitally without disturbing the positioning of the mouse. Immediately following antibody injection, serial CT scans were acquired at 7-minute intervals for up to 49 minutes after injection or until death. Analysis was performed in 3D Slicer (85) (version 4.11.20200930). Briefly, we used the Chest Imaging Platform Extension (revision eefe2ba) to generate the Region of Interest (ROI) and quantify the mean Hounsfield units (HU) (representing density, *i.e.*, increases in edema content in the airspace are shown as increases in HU) values for the lung. For representation, basal HU values were subtracted from subsequent scans. 3D volume renders of the lung and edema volume were calculated using Horos v. 3.6.6 (The Horos Project).

Ex vivo NET formation assay with human neutrophils

Whole blood was obtained from three healthy volunteers (age: 20-40, males and females) with informed consent and approval by the IRB of CSHL (IRB-13-025). The blood was

collected by venipuncture into a BD Vacutainer EDTA tube and red blood cells were lysed using ACK lysing buffer (Gibco, #A1049201). Plating and stimulations were done as for mouse neutrophils (see "*Ex vivo NET formation assays with mouse neutrophils*" section above).

IL-1β measurement in the lung

Lungs were collected and snap-frozen from control mice (treated with low-dose LPS but not injected with anti-H2d antibodies) and from TRALI-induced mice treated with vehicle or disulfiram, 40 minutes after TRALI induction. Pieces of lung tissue (50 mg) were transferred to tubes containing 500 µl of PBS, homogenized at 4ºC and centrifuged at 2000 RPM for 5min. Cell-free supernatants were transferred to new tubes and used to determine mouse IL-1β levels by ELISA (R&D Systems, #DY401-05) according to the manufacturer's instructions.

Bronchoaveolar lavage fluid (BALF) protein quantification

For BALF extraction, mice were euthanized in CO_2 chambers and the trachea was exteriorized. A silk thread was inserted behind the trachea, then the trachea was hemisected transversally to allow introduction of a 20G catheter (Exel Safelet catheter 20Gx1", Exelint, USA) that was then knotted to the trachea using the silk thread. Then, 1mL of saline was introduced into the lungs, carefully recovered, and placed in a sterile 1.5mL tube on ice. A total of 500µl of BALF was then centrifuged (300 x g, 10 minutes, 4ºC) and the supernatant aliquoted and frozen at -80ºC. Protein content was measured using the Pierce BCA Protein Assay Kit (Thermo Fisher) according to the manufacturer's instructions using 1:10 diluted BALF.

SARS-CoV-2 propagation, titration, and infection

SARS-CoV-2 isolate USA-WA1/2020 (NR-52281) was provided by the Center for Disease Control and Prevention and obtained through BEI Resources, NIAID, NIH. SARS-CoV-2 was propagated in Vero E6 cells in DMEM supplemented with 2% FBS, 4.5 g/L D-glucose, 4 mM L-glutamine, 10 mM Non-Essential Amino Acids, 1 mM Sodium Pyruvate and 10 mM HEPES using a passage-2 stock of virus. Three days after infection, supernatant containing propagated virus was filtered through an Amicon Ultra 15 (100kDa) centrifugal filter (Millipore Sigma) at ~4000 rpm for 20 minutes. Flow through was discarded and virus was resuspended in DMEM supplemented as described above. Infectious titers of SARS-CoV-2 were determined by plaque assay in Vero E6 cells in Minimum Essential Media supplemented with 2% FBS, 4 mM L-glutamine, 0.2% BSA, 10 mM HEPES and 0.12% NaHCO3 and 0.7% agar. All work involving live SARS-CoV-2 was performed in the CDC/USDA-approved BSL-3 facility of the Icahn School of Medicine at Mount Sinai in accordance with institutional biosafety requirements.

SARS-CoV-2 infections of Hamsters

3-5-week-old male golden hamsters (*Mesocricetus auratus*) were obtained from Jackson Laboratory. Hamsters were acclimated to the CDC/USDA-approved BSL-3 facility of the Global Health and Emerging Pathogens Institute at the Icahn School of Medicine at Mount Sinai for 2-4 days. All animal procedures were authorized by the Icahn School of Medicine at Mount Sinai. Before intranasal infection, hamsters were anesthetized by intraperitoneal injection with a ketamine HCl/xylazine solution (4:1). Hamsters were intranasally inoculated with 10^3 pfu of SARS-CoV-2 in PBS (or PBS only as a control) in a total volume of 100 μl.

On the day before infection (PRE) or the day following infection (POST), and up to the end of the experiments, animals were treated daily by intraperitoneal injection with disulfiram (or vehicle), at a dose of 150 mg/kg in 0.5 mL of sesame oil as vehicle. For dexamethasone treatment, hamsters were subcutaneously injected daily starting 1 day post infection with 0.2 mg/kg of Dexamethasone. In all cases, 6 days post-infection hamsters were euthanized, and lungs were collected (we chose day 6 post-infection as it is the time point at which the effects on the lung are most severe, based on out previous experience with the model). For lungs analyzed by immunofluorescence staining, hamsters were perfused with 60 ml of ice-cold PBS before tissue collection and collected lungs were immediately placed in 10% nonbuffered formalin (NFB) and fixed for 24 hours. For transcriptomic analysis, collected lungs were placed in TRIzol for further RNA extraction.

RNA sequencing of golden hamster lungs

Hamster total RNA was extracted in TRIzol (Invitrogen) and DNase I treated using Directzol RNA Miniprep kit (Zymo Research) according to the manufacturer's instructions. RNAseq libraries of polyadenylated RNA were prepared using TruSeq Stranded mRNA Library Prep Kit (Illumina) according to the manufacturer's instructions. cDNA libraries were sequenced using an Illumina NextSeq 500 platform. The sequencing reads were cleaned by trimming adapter sequences and low-quality bases using cutadapt v1.9.1 30, and were aligned to the hamster reference genome (downloaded from Ensembl, accession#: GCA 000349665) plus SARS-Cov-2 genome using HISAT2 2.1.0. Raw gene counts were quantified using HTSeq-count v0.11.2. Golden Hamster ensembl genes were matched to homologous external gene names, human homolog ensembl genes, and human associated homolog gene names using BioMart. OrthoFinder was used to generate orthologous human ensembl gene ids and gene names. Differential expression analysis was performed using DESeq2 v1.22.2 33. Regularized log transformation was applied to convert count data to log2 scale. Sample-to-

sample distance matrix was calculated based on the transformed log-scaled count data using R dist function. Multidimensional scaling (MDS) was performed on the distance matrix using R cmdscale function.

Further analyses were performed using R 4.0.4 ("Lost Library Book") and Bioconductor 3.12. Briefly, GO terms were obtained with gProgileR, using a max p-value of 0.05, and false discovery rate as the correction method. Up- and down-regulated gene lists were also analyzed using gProgileR with the same settings. Reactome pathway analysis was performed using the enrichPathway function of the ReactomePA library, using the ENTREZ nomenclature (mapped with the mapIds function of the AnnotationDb library) of the same lists used for the GO terms, with a q-value and p-value cutoff of 0.05 in both cases. Only pathways with adjusted p-value under 0.05 were kept. Volcano plots were represented using the EnhancedVolcano library, with a fold change cutoff of 2 and a p-value cutoff of 0.05. Reactome pathway clustering was performed using pathfinder: first the run_pathfindR function was run using the same input lists as before, on the Reactome gene set. Then, we used the cluster_enriched_terms function to perform the actual clustering of the reactome pathways. For KEGG pathways the procedure was similar but using the corresponding gene set. Top genes were extracted with dplyr. SARS-CoV-2 Infection and interferon signaling gene lists were obtained using the viewPathway function of the ReactomePA library. To compare the datasets from hamsters pre-treated or treated at the time of infection with SARS-CoV-2, we used the CompGO library. Briefly, functional annotation was acquired using DAVIDWebService by the getFnAnot_genome of the CompGO package for both datasets. Then, the comparison of the Z-scores was performed using the compareZscores function and Z-scores correlation plot and sliding Jaccard plots were exported using CompGO. The session used the following libraries: limma (3.46.0), edgeR (3.32.1), tximport (1.18.0), edgeR (3.32.1), sva (3.38.0), RColorBrewer (1.1-2), pheatmap (1.0.12), biomaRt (2.46.3), ggplot2 (3.3.3), gplots (3.1.1), ggfortify (0.4.11), NMF (0.23.0), cluster (2.1.1), fpc (2.2-9), plyr (1.8.6), dplyr (1.0.5), pvclust (2.2-0), ggrepel (0.9.1), amap (0.8-18), gProfileR

(0.7.0), xtable (1.8-4), ggpubr (0.4.0), tidyr (1.1.3), DESeq2 (1.30.1), ReactomePA (1.34.0), stringr (1.4.0), Org.Hs.eg.db (3.12.0), pathfindR (1.6.1), CompGO (1.26), EnhancedVolcano (1.8.0) and GeneBook (1.0). Code available upon request.

SARS-CoV-2 nucleocapsid protein quantification in infected lungs

Standard procedures were followed to perform immunoblotting. Briefly, 90μg total protein from each lung lysate sample (uninfected control, infected untreated, infected pretreated with disulfiram, infected post-treated with disulfiram) harvested at day 6 after infection was electrophoresed on 4-20% Mini-PROTEAN® TGX™ Precast Protein Gels (#4561094, Bio-Rad) and transferred onto a nitrocellulose membrane using the iBlot 2® Dry Blotting System (#IB2001, Invitrogen). Membranes were then blocked with 5% Non-fat dry milk in 0.1% Tween-20 Tris-Buffered Saline (TBS-T) and incubated with anti-SARS-CoV-2 nucleocapsid protein primary antibody (Abcam, #ab273167, concentration of 2ug/mL) overnight on a rocking platform at 4°C. Membranes were then incubated with mouse monoclonal [SB62a] anti-Rabbit IgG light chain (HRP) (Abcam, #ab99697, diluted 1:5,000) for one hour at room temperature before proceeding with immunodetection. HRP conjugated secondaries were visualized by incubating with Radiance ECL (Azure Biosystems, #AC2204) for 2 minutes and imaged an Azure 300 Chemiluminescent Western Blot Imaging System (Azure Biosystems). Membranes were then stripped using Restore™ Western Blot Stripping Buffer (#21059, Thermo Fisher Scientific) for 20 minutes at room temperature, washed with TBS-T, and re-blocked with 5% Non-fat dry milk in 0.1% TBS-T before probing with anti-ß-actin (C4) primary antibody (Santa Cruz Biotechnology, #sc-47778, diluted 1:500) overnight on a rocking platform at 4°C. Membranes were then incubated with IRDye® 800CW near-infrared fluorescent secondary antibody, (LI-COR, #926-32210, diluted 1:10,000) and were detected using an Odyssey® Classic Imaging System (LI-COR) and quantified using Image Studio Lite version 5.2.5 (LI-COR). To quantify, background from each image of the blot was

subtracted from the signal of the SARS-CoV-2 nucleocapsid (MW: 50kd) and ß-actin (MW: 42kd) proteins. Then, for each lysate sample run on a single blot (uninfected control, infected untreated, infected pretreated with disulfiram, infected post-treatment with disulfiram) the SARS-CoV-2 nucleocapsid signal was normalized to the ß-actin signal of the same lysate.

Golden hamster lung viral load quantification by real-time PCR

A single lung lobe was directly homogenized in 1 mL of TRIzol reagent (Invitrogen) and RNA was extracted following the manufacturer's protocol. 200 ng of RNA were used for one-step RT-qPCR (NEB Luna Universal One-Step RT-qPCR Kit). The reaction mix contained the kit's master mix, $10\mu M$ of each forward (5'-CTCTTGTAGATCTGTTCTCTAAACGAAC-3') and reverse primer (5'-GGTCCACCAAACGTAATGCG-3'), 0.5M betaine and $10\mu g$ BSA in $10\mu l$ final volume. The cycling conditions were $55^{\circ}C$ for 10 minutes, followed by 45 cycles of $95^{\circ}C$ for 10 seconds and $60^{\circ}C$ for 30 seconds, and a final melt curve in a Roche light cycler 480 II instrument.

Analysis of hamster lung slides

Hematoxylin & eosin (H&E) or Masson Trichrome-stained lung slides from disulfiram- or vehicle-treated hamsters were evaluated using QuPath (86) software (version 0.2.3) for quantitative pathology and bioimage analysis. The infiltrated area was calculated using QuPath's multilayer perceptron (MLP-ANN) pixel classifier trained to the area of highly packed hematoxylin content and compared to total lung area (excluding alveolar space, also calculated using pixel classifiers). The number of neighbors was calculated to generate a cell density map using the QuPath Cell Detection module in H&E-stained slides. To calculate cellularity per area, the total number of cells was compared to total lung area, excluding the alveolar space. Perivascular fibrosis was calculated by measuring the width of the fibrous

27

perivascular tissue normalized to the lumen diameter of the same vessel; we measured 10 individual vessels for each lung section, and then averaged them to obtain the mean value per lung. Finally, to quantify neutrophil numbers, unstained sections were deparaffinated, as previously reported (67) and stained for MPO (Cat. #AF3667, R&D Systems) as stated above (see "*Ex vivo NET formation assays with mouse neutrophils*" for instance). Slides were imaged using a Leica SP8 Microscope, and neutrophil numbers were determined using the Imaris (Bitplane) spots tool and normalized to tissue area.

Data availability

We used the hamster reference genome from Ensembl, accession number: GCA 000349665. The SARS-CoV-2 infected golden hamster RNA-sequencing has been uploaded to GEO, accession number: GSE180417. All other pieces of data are available upon request. The ImageJ macro for ex vivo NET quantification is available in FigShare (DOI: 10.6084/m9.figshare.14401958). RNA-seq analysis code is available upon request.

Statistical analysis

Unless otherwise indicated, data are represented as mean values ± standard error of the mean (SEM). Paired or unpaired Student's t-test was used to compare two groups, and more than two data sets were compared using one-way analysis of variance (ANOVA) with Tukey's post-test. Where applicable, normality was estimated using D'Agostino & Pearson or Shapiro-Wilk normality test. Log-rank (Mantel-Cox) analysis was used for Kaplan-Meier survival curves. The precise tests used are stated in the Figure legend. No samples were excluded. All statistical analyses, except for RNA-seq analysis (see "RNA sequencing" section above), were performed using Prism v8 (GraphPad Software, California, USA). A p-value below 0.05 was considered statistically significant; non-significant differences (n.s.) are indicated in the figures.

Study approval

All experiments with mice were conducted in accordance with procedures approved by the Institutional Animal Care and Use Committee (IACUC) at CSHL and the National Institutes of Health (NIH) Guide for the Care and Use of Laboratory Animals. All experiments with hamsters were performed at the Global Health and Emerging Pathogens Institute at the Icahn School of Medicine at Mount Sinai and were authorized by the Icahn School of Medicine at Mount Sinai.

Author contributions

J.M.A., L.C., J.D.P., Y.B., V.C., J.R.M. and M.S. performed experiments. J.M.A., S.H. and D.R. performed bioinformatic analyses. J.M.A., B. R. T., S.L., R.E.S., and M.E. designed and supervised experiments. J.M.A and M.E. wrote the manuscript, which was edited by all authors.

Acknowledgements

REFERENCES

1. Rubenfeld GD, Weaver J, Stern EJ. Incidence and Outcomes of Acute Lung Injury. *N. Engl. J. Med.* 2005;9.

2. Cheng OZ, Palaniyar N. NET balancing: A problem in inflammatory lung diseases. *Front. Immunol.* 2013;4(JAN):1–13.

3. Adrover JM, et al. Programmed 'disarming' of the neutrophil proteome reduces the magnitude of inflammation. *Nat. Immunol.* [published online ahead of print: January 13, 2020]; doi:10.1038/s41590-019-0571-2

4. Thomas GM, et al. Extracellular DNA traps are associated with the pathogenesis of TRALI in humans and mice. *Blood* 2012;119(26):6335–6343.

5. Branzk N, et al. Neutrophils sense microbial size and selectively release neutrophil extracellular traps in response to large pathogens. *Nat Immunol* 2015;15(11):1017–1025.

6. Brinkmann V, et al. Neutrophil Extracellular Traps Kill Bacteria. *Science* 2004;303(5663):1532–1535.

7. Narasaraju T, et al. Excessive neutrophils and neutrophil extracellular traps contribute to acute lung injury of influenza pneumonitis. *Am. J. Pathol.* 2011;179(1):199–210.

8. Zhu L, et al. High Level of Neutrophil Extracellular Traps Correlates with Poor Prognosis of Severe Influenza A Infection. *J. Infect. Dis.* 2018;217(3):428–437.

9. Döring Y, Soehnlein O, Weber C. Neutrophils Cast NETs in Atherosclerosis. *Circ. Res.* 2014;114(6):931–934.

10. Cui B-B, et al. Neutrophil extracellular traps in sterile inflammation: the story after dying?. *Autoimmunity* 2012;45(8):593–596.

11. Binet F. Neutrophil Extracellular Traps Target Senescent Vasculature For Tissue Remodeling in Retinopathy2020;5356. doi:10.1126/science.aay5356

12. Huang H, et al. Damage-associated molecular pattern-activated neutrophil extracellular trap exacerbates sterile inflammatory liver injury. *Hepatology* 2015;62(2):600–614.

13. Slaba I, et al. Imaging the dynamic platelet-neutrophil response in sterile liver injury and repair in mice. *Hepatology* 2015;62(5):1593–1605.

14. Saffarzadeh M, et al. Neutrophil extracellular traps directly induce epithelial and endothelial cell death: A predominant role of histones. *PLoS ONE* 2012;7(2). doi:10.1371/journal.pone.0032366

15. Silvestre-Roig C, et al. Externalized histone H4 orchestrates chronic inflammation by inducing lytic cell death. *Nature* 2019;569(7755):236–240.

16. Abrams ST, et al. Circulating histones are mediators of trauma-associated lung injury. *Am. J. Respir. Crit. Care Med.* 2013;187(2):160–169.

17. Zuo Y, et al. Neutrophil extracellular traps (NETs) as markers of disease severity in COVID-19. *JCI Insight* [published online ahead of print: 2020]; doi:10.1101/2020.04.09.20059626

18. Veras FP, et al. SARS-CoV-2-triggered neutrophil extracellular traps mediate COVID-19 pathology. *J. Exp. Med.* [published online ahead of print: 2020]; doi:10.1084/jem.20201129

19. Yaqinuddin A, Kashir J. Novel therapeutic targets for SARS-CoV-2-induced acute lung injury: Targeting a potential IL-1β/neutrophil extracellular traps feedback loop. *Med. Hypotheses* [published online ahead of print: 2020]; doi:10.1016/j.mehy.2020.109906

20. Lefrançais E, et al. Maladaptive role of neutrophil extracellular traps in pathogen-induced lung injury. *JCI Insight* 2018;3(3):1–15.

21. Middleton EA, et al. Neutrophil extracellular traps contribute to immunothrombosis in COVID-19 acute respiratory distress syndrome. *Blood* 2020;136(10):1169–1179.

22. Tomar B, et al. Neutrophils and Neutrophil Extracellular Traps Drive Necroinflammation in COVID-19. *Cells* [published online ahead of print: 2020]; doi:10.3390/cells9061383

23. Gómez-Moreno D, Adrover JM, Hidalgo A. Neutrophils as effectors of vascular inflammation. *Eur. J. Clin. Invest.* 2018;48(January):1–14.

24. Soltani M, Mansour S. Biventricular Thrombi Associated With Myocardial Infarction in a Patient With COVID-19. *Can. J. Cardiol.* [published online ahead of print: 2020]; doi:10.1016/j.cjca.2020.06.016

25. Manne BK, et al. Platelet gene expression and function in patients with COVID-19. *Blood* [published online ahead of print: 2020]; doi:10.1182/blood.2020007214

26. Veras FP, et al. SARS-CoV-2-triggered neutrophil extracellular traps mediate COVID-19 pathology. *J. Exp. Med.* [published online ahead of print: 2020]; doi:10.1084/jem.20201129

27. Barnes BJ, et al. Targeting potential drivers of COVID-19: Neutrophil extracellular traps.. *J. Exp. Med.* 2020;217(6):1–7.

28. Leppkes M, et al. Vascular occlusion by neutrophil extracellular traps in COVID-19.. *EBioMedicine* 2020;58:102925.

29. Guiducci E, et al. Candida albicans-Induced NETosis Is Independent of Peptidylarginine Deiminase 4. *Front. Immunol.* 2018;9:1573.

30. Sollberger G, et al. Gasdermin D plays a vital role in the generation of neutrophil extracellular traps. *Sci. Immunol.* 2018;3(26). doi:10.1126/sciimmunol.aar6689

31. Chen KW, et al. Noncanonical inflammasome signaling elicits gasdermin D–dependent neutrophil extracellular traps. *Sci. Immunol.* 2018;3(26):eaar6676.

32. Hu JJ, et al. FDA-approved disulfiram inhibits pyroptosis by blocking gasdermin D pore formation. *Nat. Immunol.* 2020;21(7):736–745.

33. Schmidt FI, Latz E. Jack of all trades inhibits inflammation (in sober people). *Nat. Immunol.* 2020;21(7):718–719.

34. Looney MR, Gilliss BM, Matthay MA. Pathophysiology of transfusion-related acute lung injury. *Curr. Opin. Hematol.* 2010;17(5):418–423.

35. Eneanya DI, et al. The Actions and Metabolic Fate of Disulfiram. *Annu. Rev. Pharmacol. Toxicol.* 1981;21(1):575–596.

36. Looney MR, et al. Neutrophils and their Fcγ receptors are essential in a mouse model of transfusion-related acute lung injury. *J. Clin. Invest.* 2006;116(6):1615–1623.

37. Sreeramkumar V, et al. Neutrophils scan for activated platelets to initiate inflammation. *Science* 2014;346(6214):1234–1238.

38. Caudrillier A, et al. Platelets induce neutrophil extracellular traps in transfusion-related acute lung injury. *J. Clin. Invest.* 2012;122(7):2661–2671.

39. Knight JS, et al. Peptidylarginine deiminase inhibition is immunomodulatory and vasculoprotective in murine lupus. *J. Clin. Invest.* 2013;123(7):2981–2993.

40. Knight JS, et al. Peptidylarginine Deiminase Inhibition Reduces Vascular Damage and Modulates Innate Immune Responses in Murine Models of Atherosclerosis. *Circ. Res.* 2014;114(6):947–956.

41. Coffelt SB, et al. IL-17-producing γδ T cells and neutrophils conspire to promote breast cancer metastasis. *Nature* 2015;522(7556):345–348.

42. Manzenreiter R, et al. Ultrastructural characterization of cystic fibrosis sputum using atomic force and scanning electron microscopy. *J. Cyst. Fibros.* 2012;11(2):84–92.

43. Martínez-Alemán SR, et al. Understanding the entanglement: Neutrophil extracellular traps (NETs) in cystic fibrosis. *Front. Cell. Infect. Microbiol.* 2017;7(APR):1–7.

44. Fuchs TA, Brill A, Wagner DD. Neutrophil extracellular trap (NET) impact on deep vein thrombosis. *Arterioscler. Thromb. Vasc. Biol.* 2012;32(8):1777–1783.

45. Borissoff JI, Ten Cate H. From neutrophil extracellular traps release to thrombosis: An overshooting host-defense mechanism?. *J. Thromb. Haemost.* 2011;9(9):1791–1794.

46. Guo T, et al. Cardiovascular Implications of Fatal Outcomes of Patients with Coronavirus Disease 2019 (COVID-19). *JAMA Cardiol.* [published online ahead of print: 2020]; doi:10.1001/jamacardio.2020.1017

47. Bonow RO, et al. Association of Coronavirus Disease 2019 (COVID-19) with Myocardial Injury and Mortality. *JAMA Cardiol.* 2020; doi:10.1001/jamacardio.2020.1105

48. Klok FA, et al. Incidence of thrombotic complications in critically ill ICU patients with COVID-19. *Thromb. Res.* [published online ahead of print: 2020]; doi:10.1016/j.thromres.2020.04.013

49. Becker RC. COVID-19 update: Covid-19-associated coagulopathy. *J. Thromb. Thrombolysis* [published online ahead of print: 2020]; doi:10.1007/s11239-020-02134-3

50. Xiao Z, Théroux P, Frojmovic M. Modulation of platelet-neutrophil interaction with pharmacological inhibition of fibrinogen binding to platelet GPIIb/IIIa receptor. *Thromb. Haemost.* 1999;81(2):281–285.

51. King BO, et al. Tirofiban administration attenuates platelet and platelet-neutrophil conjugation but not neutrophil degranulation during in vitro vad circulation. *ASAIO J.* 2001;47(3):282–287.

52. Imai M, et al. Syrian hamsters as a small animal model for SARS-CoV-2 infection and countermeasure development. *Proc. Natl. Acad. Sci. U. S. A.* 2020;117(28):16587–16595.

53. Samuel CE. Antiviral Actions of Interferons. *Clin. Microbiol. Rev.* 2001;14(4):778–809.

54. Abdolvahab MH. Potential role of interferons in treating COVID-19 patients. *Int. Immunopharmacol.* 2021;15.

55. Ulgen E, Ozisik O, Sezerman OU. pathfindR: An R Package for Comprehensive Identification of Enriched Pathways in Omics Data Through Active Subnetworks. *Front. Genet.* 2019;10:858.

56. Gregoriano C, et al. Activation of vasopressin system during COVID-19 is associated with adverse clinical outcomes: an observational study. *J. Endocr. Soc.* 2021;bvab045.

57. Diep P-T, Talash K, Kasabri V. Hypothesis: Oxytocin is a direct COVID-19 antiviral. *Med. Hypotheses* 2020;145:110329.

58. Adamson IYR, Bowden DH. The Pathogenesis of Bleomycin-Induced Pulmonary Fibrosis in Mice1974;77(2):14.

59. The RECOVERY Collaborative Group. Dexamethasone in Hospitalized Patients with Covid-19. *N. Engl. J. Med.* 2021;384(8):693–704.

60. Papayannopoulos V. Neutrophil extracellular traps in immunity and disease. *Nat. Rev. Immunol.* 2017;1–14.

61. Barth K, Malcolm R. Disulfiram: An Old Therapeutic with New Applications. *CNS Neurol. Disord. - Drug Targets* 2010;9(1):5–12.

62. Silva CM, et al. Gasdermin D inhibition prevents multiple organ dysfunction during sepsis by blocking NET formation. *Blood* 2021;blood.2021011525.

63. Nicolás-Ávila JÁ, Adrover JM, Hidalgo A. Neutrophils in Homeostasis, Immunity, and Cancer. *Immunity* 2017;46(1):15–28.

64. Jorch SK, Kubes P. An emerging role for neutrophil extracellular traps in noninfectious disease. *Nat. Med.* 2017;23(3):279–287.

65. Fuchs TA, et al. Extracellular DNA traps promote thrombosis.. *Proc. Natl. Acad. Sci. U. S. A.* 2010;107(36):15880–5.

66. Park J, et al. Cancer cells induce metastasis-supporting neutrophil extracellular DNA traps. *Sci. Transl. Med.* 2016;8(361):361ra138-361ra138.

67. Albrengues J, et al. Neutrophil extracellular traps produced during inflammation awaken dormant cancer cells in mice. *Science* 2018;361(6409):eaao4227.

68. Demers M, Wagner DD. NETosis: A new factor in tumor progression and cancer-associated thrombosis. *Semin. Thromb. Hemost.* 2014;40(3):277–283.

69. Skrott Z, et al. Alcohol-abuse drug disulfiram targets cancer via p97 segregase adaptor NPL4. *Nature* 2017;552(7684):194–199.

70. Kolaczkowska E, et al. Molecular mechanisms of NET formation and degradation revealed by intravital imaging in the liver vasculature.. *Nat. Commun.* 2015;6:1–13.

71. de Buhr N, et al. Degraded neutrophil extracellular traps promote the growth of Actinobacillus pleuropneumoniae. *Cell Death Dis.* 2019;10(9):657.

72. Castanheira FVS, Kubes P. Neutrophils and NETs in modulating acute and chronic inflammation. *Blood* 2019;133(20):2178–2185.

73. Evavold CL, et al. The Pore-Forming Protein Gasdermin D Regulates Interleukin-1 Secretion from Living Macrophages. *Immunity* 2018;48(1):35-44.e6.

74. Huet T, et al. Anakinra for severe forms of COVID-19: a cohort study. *Lancet Rheumatol.* 2020;2(7):e393–e400.

75. Khan FA, et al. Systematic review and meta-analysis of anakinra, sarilumab, siltuximab and tocilizumab for COVID-19. *Thorax* 2021;thoraxjnl-2020-215266.

76. Jin Z, et al. Structure of Mpro from SARS-CoV-2 and discovery of its inhibitors. *Nature* 2020;582(7811):289–293.

77. Andoh Y, et al. Perivascular Fibrosis of Muscular Pulmonary Arteries in Chronic Obstructive Pulmonary Disease. *Chest* 1992;102(6):1645–1650.

78. Suzuki YJ, et al. COVID-19 patients may become predisposed to pulmonary arterial hypertension. *Med. Hypotheses* 2021;147:110483.

79. Ytrehus K, et al. Perivascular fibrosis and the microvasculature of the heart. Still hidden secrets of pathophysiology?. *Vascul. Pharmacol.* 2018;107:78–83.

80. Jiang K, et al. Gasdermin D inhibition confers antineutrophil mediated cardioprotection in acute myocardial infarction. *J. Clin. Invest.* [published online ahead of print: November 9, 2021]; doi:10.1172/JCI151268

81. Buckingham SC, et al. A Randomized, Double-Blind, Placebo-Controlled Trial of Dexamethasone in Severe Respiratory Syncytial Virus (RSV) Infection: Effects on RSV Quantity and Clinical Outcome. *J. Infect. Dis.* 2002;185(9):1222–1228.

82. Tamburin S, et al. COVID-19 and related symptoms in patients under disulfiram for alcohol use disorder. *Intern. Emerg. Med.* 2021;(0123456789):2–4.

83. Fillmore N, et al. Disulfiram use is associated with lower risk of COVID-19: A retrospective cohort study. *PLOS ONE* 2021;16(10):e0259061.

84. Adrover JM, et al. A Neutrophil Timer Coordinates Immune Defense and Vascular Protection. *Immunity* 2019;50(2):390-402.e10.

85. Fedorov A, et al. 3D Slicer as an image computing platform for the Quantitative Imaging Network. *Magn. Reson. Imaging* [published online ahead of print: 2012]; doi:10.1016/j.mri.2012.05.001

86. Bankhead P, et al. QuPath: Open source software for digital pathology image analysis. *Sci. Rep.* 2017;7(1):16878.
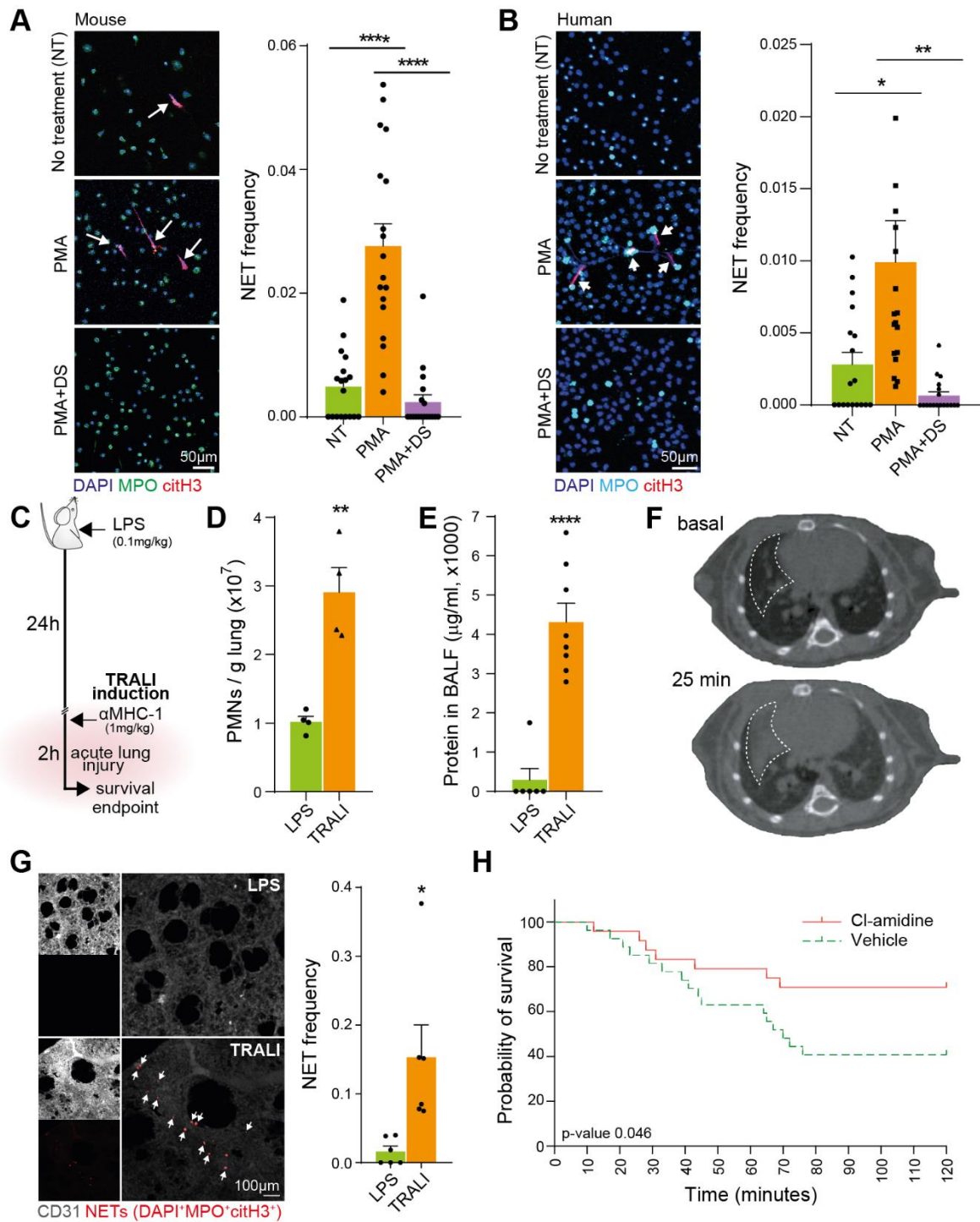
Main figure legends:

Figure 1: Disulfiram blocks neutrophil extracellular trap (NET) formation, and TRALI is a model of NET-driven lung injury. (A) Ex vivo NET formation assay of FACS-sorted mouse neutrophils, unstimulated/untreated (NT) or stimulated with 100nM of PMA or PMA + 10µM disulfiram (PMA+DS). NET frequency (NET counts normalized to neutrophil counts,

with NETs defined by the triple co-localization events of DNA, myeloperoxidase [MPO], and citrullinated histone H3 [citH3]). N = 18 random fields from 4 mice per condition. **(B)** Ex vivo NET formation assay of human neutrophils from RBC-lysed blood, unstimulated or stimulated with PMA or PMA + 10µM disulfiram (PMA+DS). N = 18 random fields from 3 healthy donors per condition. **(C)** Experimental design used to induce TRALI. **(D)** Absolute number of neutrophils (PMNs) infiltrated to the lung upon TRALI, determined by flow cytometry. N = 4 mice per group. **(E)** Protein content in the broncho-alveolar lavage fluid (BALF) as a measure of endothelial integrity. N = 6 control and 8 TRALI mice. **(F)** Representative longitudinal CT scan of a mouse subjected to TRALI showing edema formation over time (representative of CT scans from 11 independent mice). **(G)** Whole mount tissue clearing images (left, showing CD31 and NETs [arrows], defined as the triple co-localization channel of DNA, MPO, and citH3). Quantification (right) of NETs in the lungs of mice 40 min after TRALI induction or in mice treated only with LPS. N = 6 lungs per group. **(H)** Survival of mice after TRALI induction and treatment with Cl-amidine, a PAD4 inhibitor able to block NET formation, or vehicle. N = 27 (vehicle) and 24 (Cl-amidine) mice. Bars show mean ± S.E.M. *P< 0.05, **P< 0.01, ***P< 0.001; n.s., not significant, as determined by unpaired (D, E, G) two-tailed t-test analysis, one-way ANOVA with Tukey's multiple comparison test (A, B) or log-rank (Mantel–Cox) test (H).
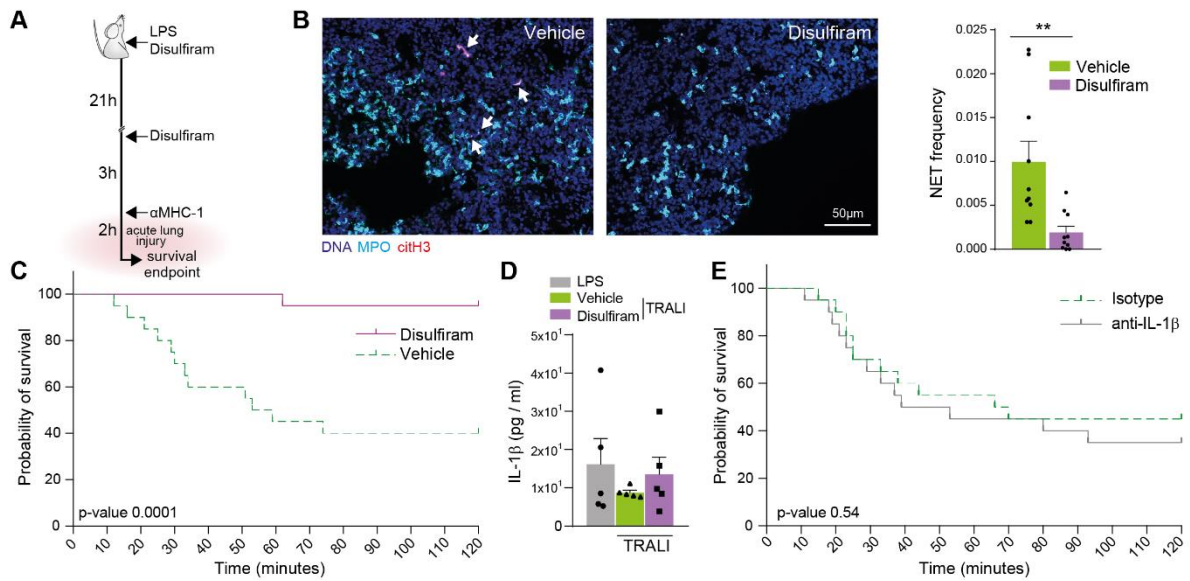
Figure 2: Disulfiram blocks NET formation in vivo and protects against acute lung injury. (A) Experimental design. **(B)** Whole mount tissue clearing images (left) and quantification (right) of NETs formed in vivo upon TRALI induction in mice treated with disulfiram or vehicle. N = 10 lung volumes from 7 mice per group. **(C)** Survival curve of mice treated with 50 mg/kg disulfiram in sesame oil 24 h and 3 h before TRALI induction. N = 20 mice per group. **(D)** IL-1β measurement in lung lysates of LPS-only-treated control mice or mice subject to TRALI induction and treated with vehicle or disulfiram. N = 5 mice per group, lungs acquired 40 min after TRALI induction. **(E)** Survival curves of mice treated intravenously with 50μg of IL-1β blocking antibodies or isotype control antibodies 5 minutes prior to TRALI induction. N = 20 mice per group. Bars show mean ± S.E.M. **P< 0.01, as determined by one-way ANOVA with Tukey's multiple comparison test (D) or unpaired two-tailed Student's t-test (B). Survival plots show the probability of survival as determined by log-rank (Mantel–Cox) test (C, E).
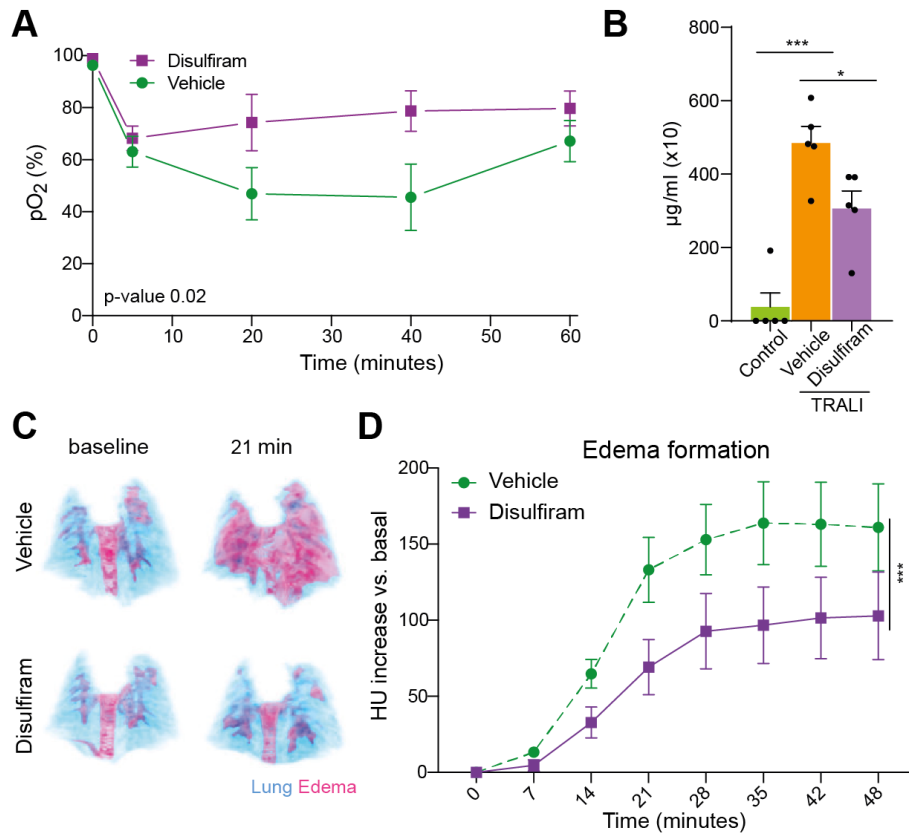
Figure 3: Disulfiram treatment improves key respiratory parameters upon TRALI induction. (A) pO$_2$ measured longitudinally on surviving mice after TRALI induction and treatment with disulfiram or vehicle. N = 4 (vehicle) and 3 (disulfiram) mice. **(B)** Protein content in the BALF of naïve mice or mice after TRALI induction and treatment with either disulfiram or vehicle. N = 5 mice per condition. **(C)** Representative projections from longitudinal CT scans of mice after TRALI induction and treatment with disulfiram or vehicle, showing the lung volume (in blue) and water-dense tissue (edema, in red). Representative of N = 10 mice per group. **(D)** Quantification of the longitudinal CT scans of mice after TRALI induction and treatment with disulfiram or vehicle. Basal HU units (prior to TRALI induction) were subtracted from all subsequent measurements to represent the increase in edema formation. N = 10 mice per group. Bars show mean ± S.E.M. *P< 0.05, ***P< 0.001; n.s., not significant, as determined by one-way ANOVA with Tukey's multiple comparison test (B) or two-way ANOVA (A, D).
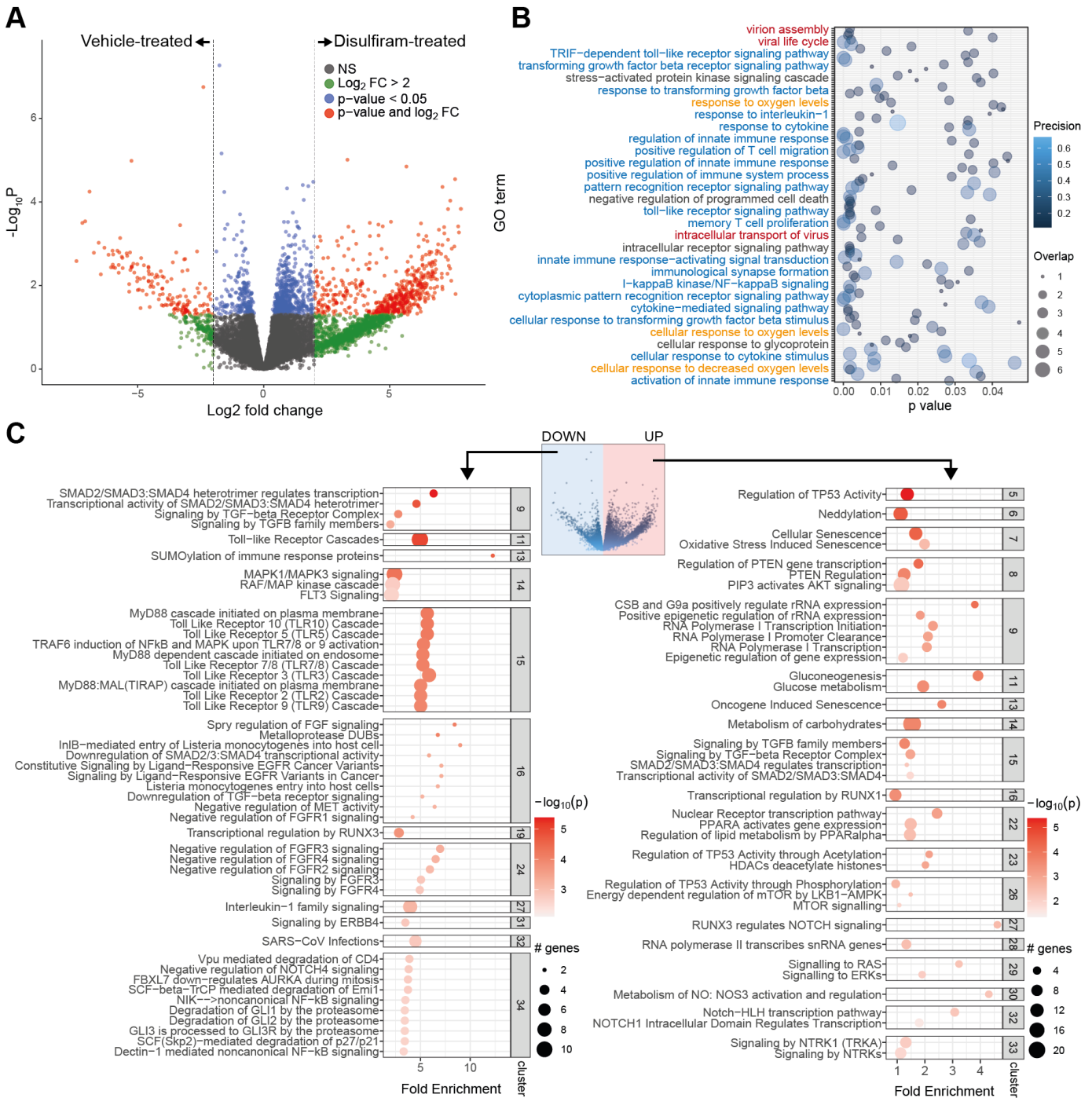
Figure 4: RNA sequencing data from lungs of infected hamsters treated with disulfiram or vehicle. (A) Volcano plot of Log₂FC (log 2 of the fold change) vs. -Log₁₀P (log 10 of the p-value) of all genes in the dataset. Positive and negative values on the x-axis represent genes upregulated and downregulated, respectively, by disulfiram treatment. Green dots show genes with a log2 fold change over 2 between conditions, blue dots represent genes with a p-value under 0.05, and red dots show those genes that have both a

log2 FC > 2 and a p-value < 0.05. **(B)** GO biological processes terms enriched in the whole differentially expressed genes list highlighting some of the terms (full list in Supplemental Table 2) related to immune functions (blue), response to oxygen levels (orange) and viral life cycle (red). **(C)** Clustering of Reactome pathways enriched in the genes downregulated (left) or upregulated (right) in response to disulfiram in SARS-CoV-2-infected golden hamsters. Some of the clusters (gray squares) are shown here (full list in Supplemental Table 4). Color and bubble size reflect the -log10 of the p-value for that pathway and the number of genes present in the dataset belonging to a particular pathway, respectively.
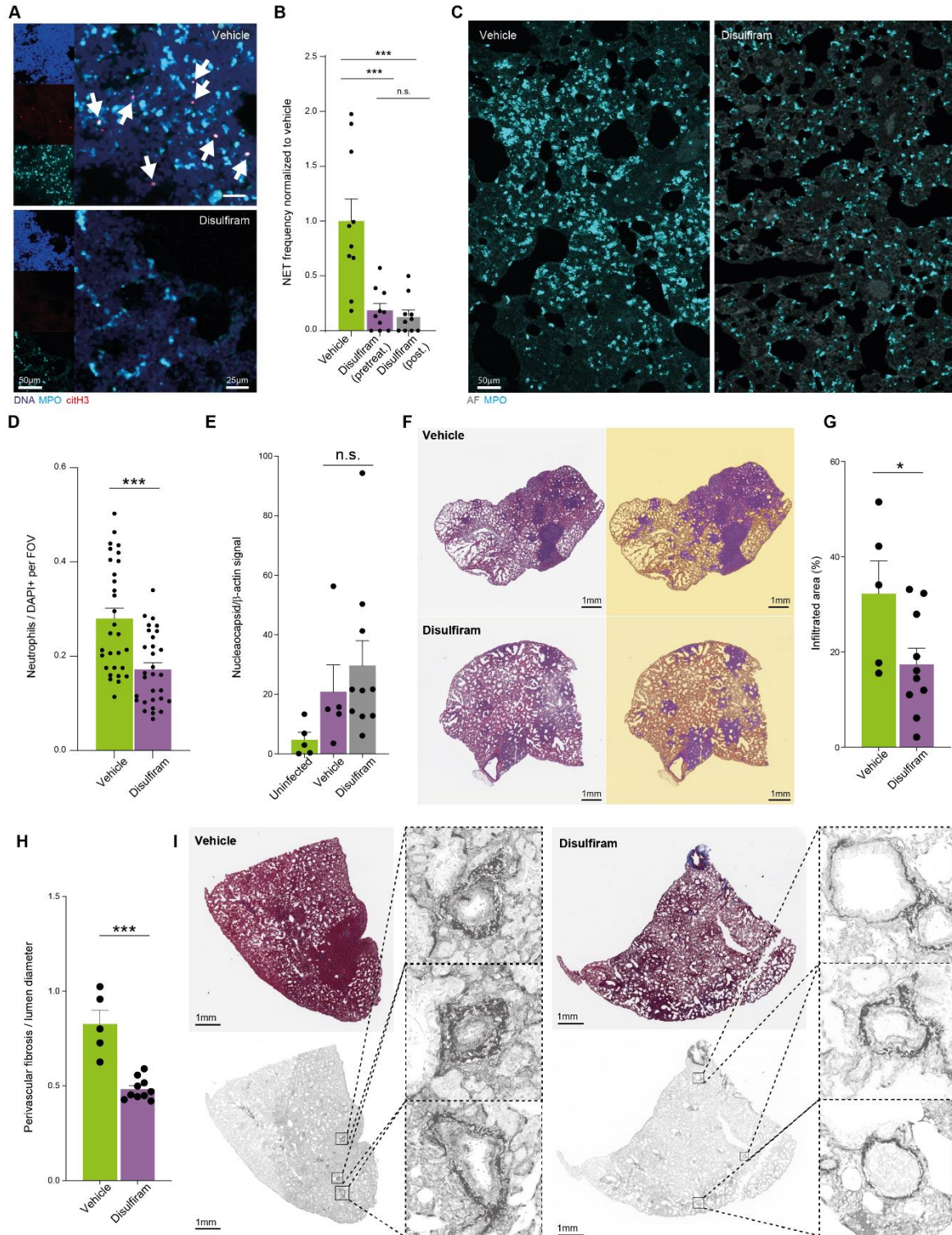
Figure 5: Disulfiram improves lung histology in a golden hamster SARS-CoV-2 infection model. (A) Representative images from whole mount cleared SARS-CoV-2-infected lungs from hamsters treated with disulfiram or vehicle. Arrows point to NETs,

defined as triple co-localization events of DNA, MPO, and citH3. Representative of 5 independent whole mounts per group. **(B)** Quantification of NETs in the lungs of SARS-CoV-2-infected hamsters. A group was started on daily disulfiram treatment 24 h prior to infection (*pretreat.*), while disulfiram was initiated in the other group one day post infection (*post.*). N = 10 lung volumes from five hamsters per group. **(C)** Representative images (showing MPO in cyan) and **(D)** quantification of neutrophil infiltration to the lungs of SARS-CoV-2-infected hamsters. N = 30 random fields from 5 lungs per group. **(E)** Quantification of SARS-CoV-2 nucleocapsid signal normalized to beta-actin (both proteins detected in lung lysates by western blot) in disulfiram- and vehicle-treated hamsters, showing that disulfiram does not affect viral load. N = 5 western blots from 3 uninfected hamsters, 5 western blots from 5 infected and vehicle-treated hamsters, and 10 blots from infected and disulfiram-treated hamsters (5 from the pre-treatment and 5 from the post-treatment groups). **(F)** Representative images (left, original image; right, detection overlay showing infiltrated area in violet) and **(G)** quantification of the heavily immune-infiltrated areas from hematoxylin and eosin-stained lungs of disulfiram- or vehicle-treated hamsters infected with SARS-CoV-2. N = 5 (vehicle) and 10 (disulfiram) lungs per group. **(H)** Quantification (mean value of 10 independent measurements per lung) and **(I)** representative images of perivascular fibrosis in the Masson trichrome-stained lungs of infected hamsters treated with disulfiram or vehicle. N = 5 (vehicle) and 10 (disulfiram) lungs per group. Bars show mean ± S.E.M. *$P < 0.05$, ***$P < 0.001$; n.s., not significant, as determined by one-way ANOVA with Tukey's multiple comparison test (A) or unpaired two-tailed t-test analysis (D, E, G, H).

Disulfiram inhibits neutrophil extracellular trap formation protecting rodents from acute lung injury and SARS-CoV-2 infection

Jose M. Adrover[1], Lucia Carrau[2], Juliane Daßler-Plenker[1], Yaron Bram[3], Vasuretha Chandar[3], Sean Houghton[4], David Redmond[4], Joseph R. Merrill[1], Margaret Shevik[1,6,7], Benjamin R tenOever[2,8], Scott Lyons[1], Robert E. Schwartz[3,5,*] and Mikala Egeblad[1,*]

Affiliations:

[1] Cold Spring Harbor Laboratory, Cold Spring Harbor, NY 11724, USA.

[2] Department of Microbiology, Icahn School of Medicine at Mount Sinai. 1468 Madison Ave. New York, NY, 10029, USA.

[3] Division of Gastroenterology and Hepatology, Department of Medicine, Weill Cornell Medicine, 1300 York Ave, New York, NY, 10065, USA.

[4] Division of Regenerative Medicine, Ansary Stem Cell Institute, Weill Cornell Medicine, New York, NY, 10065, USA

[5] Department of Physiology, Biophysics and Systems Biology, Weill Cornell Medicine, 1300 York Ave, New York, NY, 10065, USA.

[6] Medical Scientist Training Program, School of Medicine, Stony Brook University, Stony Brook, NY 11794, USA

[7] Graduate Program in Pharmacology, Stony Brook University, Stony Brook, NY 11794, USA

[8] Current address: Virology Institute, New York University, Langone Medical Center, New York, NY 10016, USA.

* Correspondence to: Mikala Egeblad, Cold Spring Harbor Laboratory, 1 Bungtown Rd, Cold Spring Harbor, NY 11721, e-mail: egeblad@cshl.edu or Robert E. Schwartz, Weill Cornell Medicine, 413 East 69th Street, New York, NY 10021, e-mail: res2025@med.cornell.edu
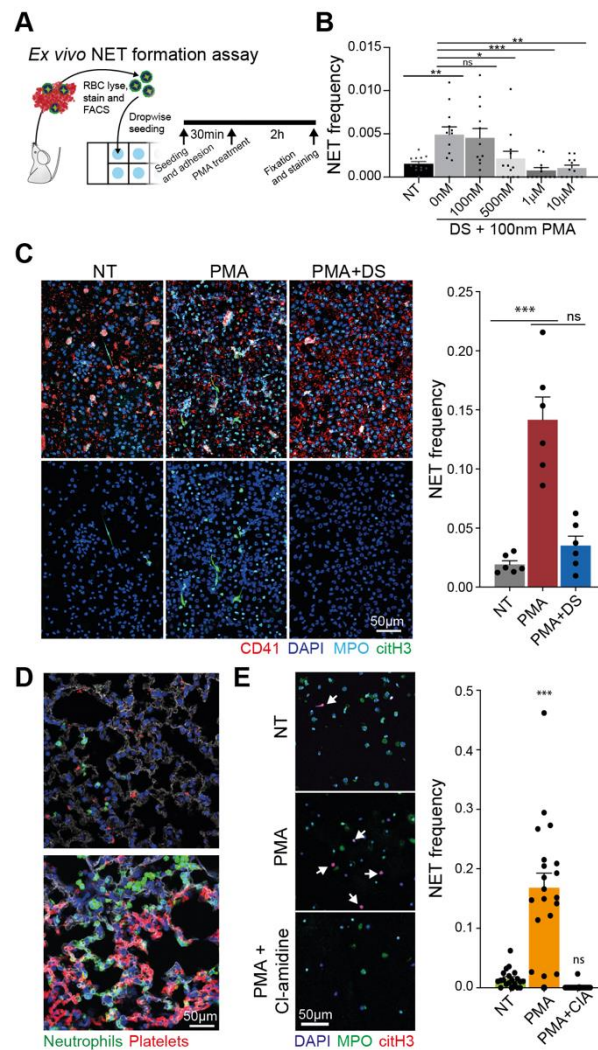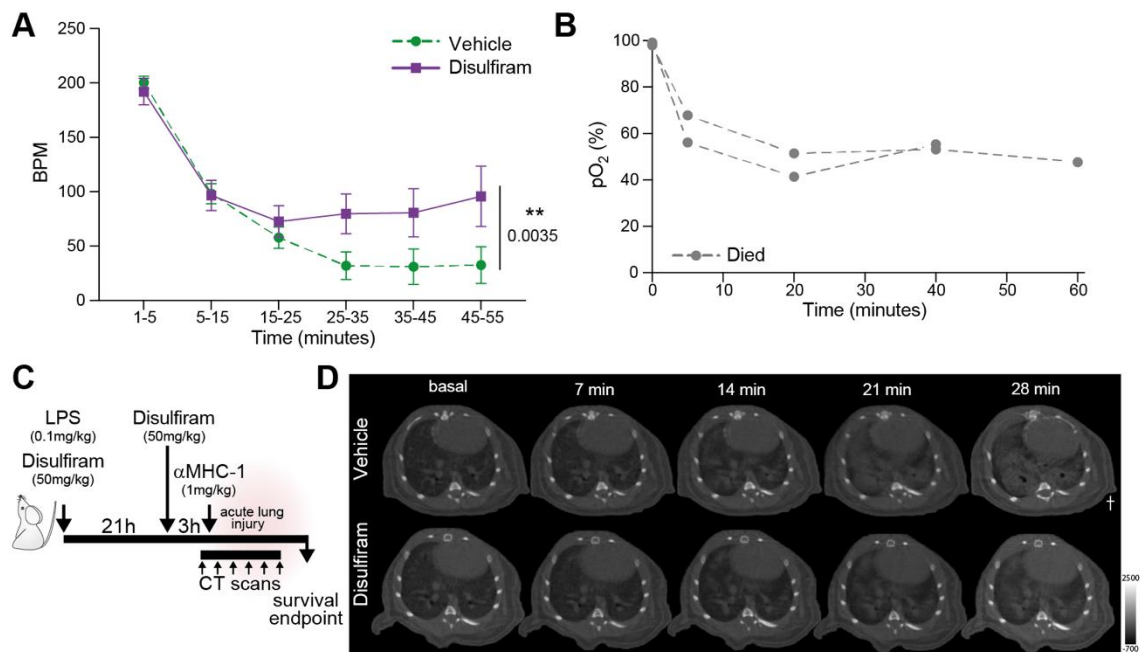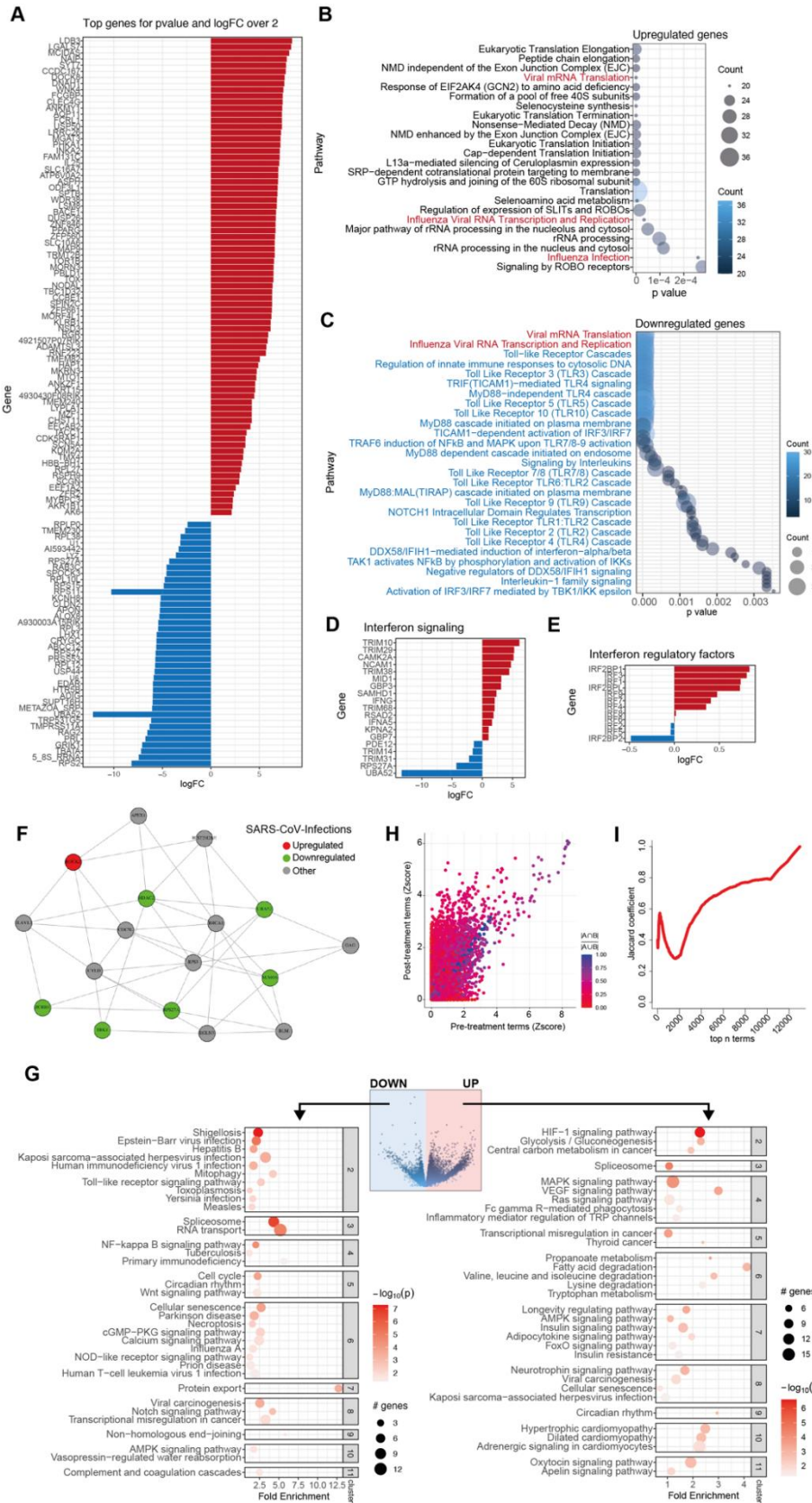
Supplemental Figure 1: Related to Figure 1. (A) Experimental design for *ex vivo* NET formation assay. **(B)** *Ex vivo* NET formation assay using mouse blood neutrophils stimulated with 100nM PMA and increasing doses of disulfiram. **(C)** Images (left) and quantification (right) of the *ex vivo* NET formation assay of red blood cell (RBC)-lysed blood neutrophils unstimulated or stimulated with 100nM of PMA or PMA + 10μM disulfiram (PMA+DS). N = 6 random fields using neutrophils from 3 independent mice per group. The top row of images shows all channels, while the bottom row shows only DAPI and citH3, for clarity. **(D)** Confocal images of lungs from mice treated with LPS only (control, top) or subjected to TRALI induction (bottom) showing neutrophils (Ly6G, green), platelets (CD41, red), laminin (white) and DAPI (blue). **(E)** *Ex vivo* NET formation assay of neutrophils that were unstimulated or stimulated with 100 nM PMA or PMA + 12mg/kg Cl-amidine (PMA+CIA). Arrows mark NETs. Bars show mean ± S.E.M, *P< 0.05, **P< 0.01, ***P< 0.001; n.s., not significant, as determined by one-way ANOVA with Tukey's multiple comparison test.
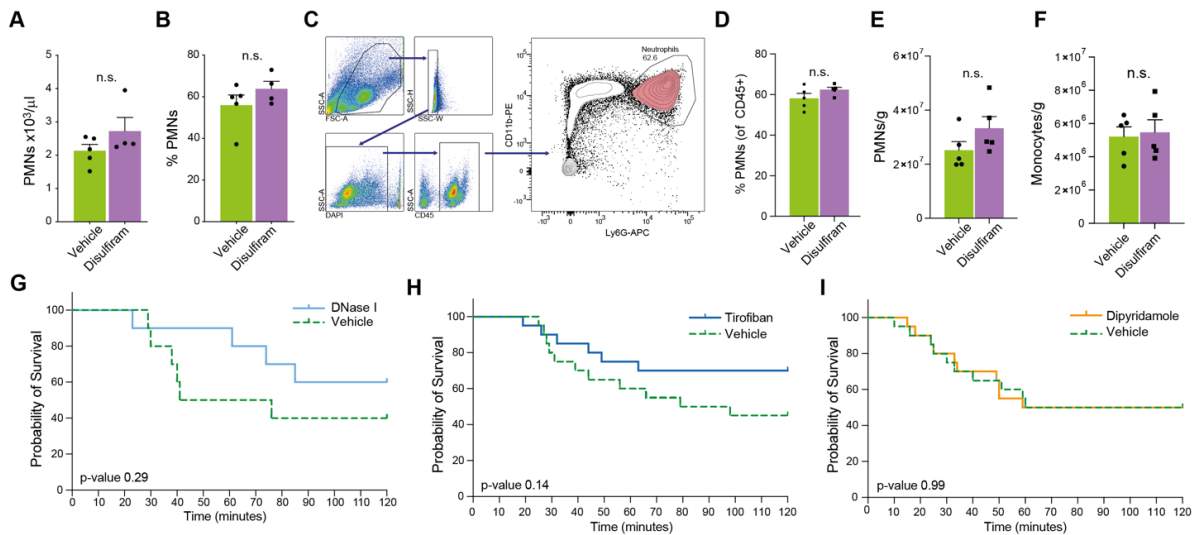
Supplemental Figure 2: Related to Figure 2. (A) Absolute number and **(B)** percentage of neutrophils in the blood of mice treated with disulfiram or vehicle, 40 minutes after TRALI induction. N = 5 vehicle- and 4 disulfiram-treated mice. **(C)** Gating strategy for the lung neutrophil quantification. **(D)** Percentage (of CD45+ leukocytes) and **(E)** Absolute numbers of neutrophils infiltrating the lungs of mice treated with disulfiram or vehicle 40 minutes after TRALI induction. N = 5 mice per group. **(F)** Absolute counts of monocytes infiltrating the lungs of mice treated with disulfiram or vehicle 40 minutes after TRALI induction. N = 5 mice per group. **(G)** Survival curves of mice treated with intranasal DNase I (200U) or vehicle 5 minutes prior to TRALI induction. N = 10 mice per group. **(H)** Survival curves of mice treated with 0.5 mg/kg of tirofiban or vehicle intravenously 1 h before TRALI induction. N = 20 mice per group. **(I)** Survival curves of mice treated intraperitoneally with 8 mg/kg dipyridamole in sesame oil or vehicle 24 and 3 h before TRALI induction, N = 20 mice per group. Bars show mean ± S.E.M, n.s., not significant, as determined by unpaired two-tailed t-test analysis (A, B, D, E, F). Survival curves show probability of survival. Statistics located at the bottom left of each graph determined by log-rank (Mantel–Cox) test (G, H, I).
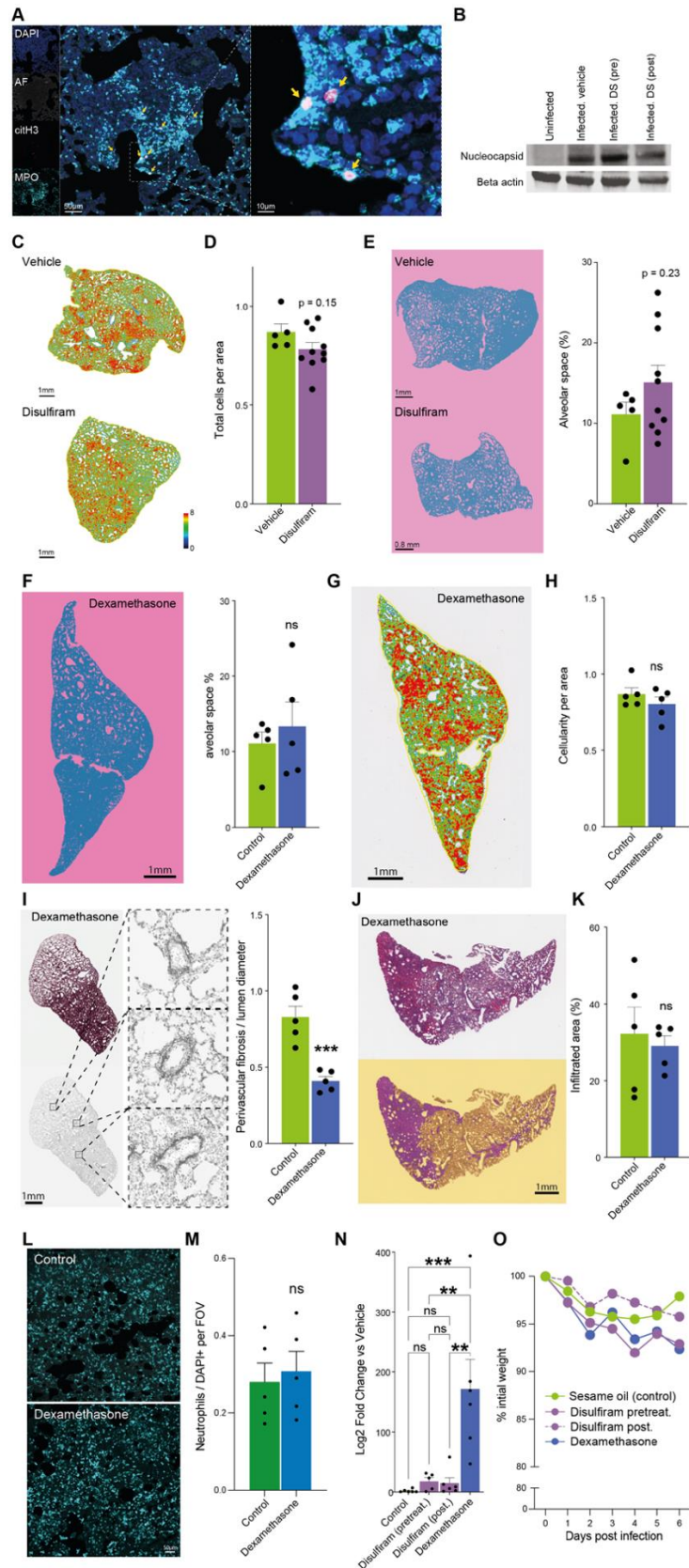
Supplemental Figure 3: Related to Figure 3. (A) Breaths per minute (BPM) over time of mice treated with disulfiram or vehicle after TRALI induction. N = 10 mice per group. **(B)** pO_2 measurement of non-surviving vehicle-treated mice upon TRALI induction. N = 2 mice (each represented by a dashed line). **(C)** Experimental design for the CT scans. **(D)** Representative images of longitudinal CT scans of mice treated with disulfiram or vehicle at indicated time after TRALI induction. Representative of 10 mice per group. Bars show mean ± S.E.M, **P< 0.01; as determined by two-way ANOVA (A).

Supplemental Figure 4: Related to Figure 5. (A) Top differentially expressed genes from the RNA-seq of the SARS-CoV-2-infected golden hamsters, showing genes enriched (red)

or repressed (blue) upon disulfiram treatment. **(B)** Reactome pathways enriched in the genes upregulated by disulfiram. **(C)** Reactome pathways enriched in the gene expression downregulated by disulfiram (partial list). **(D)** Overview of interferon signaling genes and **(E)** interferon regulatory factors in the dataset, showing gene expression enriched (red) or repressed (blue) upon disulfiram treatment. **(F)** Overview of the interaction of genes up- and down-regulated by disulfiram of the SARS-CoV-Infections pathway in our dataset. **(G)** Clustering of KEGG pathways enriched in the gene expression downregulated (left) or upregulated (right) in response to disulfiram in SARS-CoV-2-infected golden hamsters. **(H)** Scatterplot comparing the GO terms of the disulfiram pre- and post-treatments by p-value showing their similarity (Jaccard index, $|A \cap B| / |A \cup B|$). **(I)** Comparison of pre- and post-treatment functional annotation using a sliding-jaccard coefficient, showing a high overlap in the first 200 terms.

Supplemental Figure 5: Related to Figure 4. (A) Representative image of NETs in the lungs of SARS-CoV-2-infected golden hamsters. Representative of lungs from five hamsters.

AF: auto-fluorescence. Yellow arrows point to NETs. **(B)** Representative Western blot of nucleocapsid protein and beta-actin in lung lysates from the hamsters. Representative of 5 hamsters per group, except uninfected, where N = 3. **(C)** Density map (left, showing number of neighbors per cell) and **(D)** quantification of the number of cells per area in H&E-stained sections of SARS-CoV-2-infected hamsters treated with disulfiram or vehicle. N = 5 (vehicle) and 10 (disulfiram) hamsters per group. **(E)** Representative segmented images (left) and quantification (right) of open alveolar space from H&E-stained sections of SARS-CoV-2-infected hamsters treated with disulfiram or vehicle. N = 5 (vehicle) and 10 (disulfiram) hamsters per group. **(F)** Representative segmented images (left) and quantification (right) of open alveolar space from H&E-stained sections of SARS-CoV-2-infected hamsters treated with dexamethasone. N = 5 hamsters per group (controls as in panel e for reference. Note that dexamethasone treated hamsters were infected and treated at the same time as disulfiram treated hamsters). **(G)** Density map (showing number of neighbors per cell) and **(H)** quantification of the number of cells per area in H&E-stained sections of SARS-CoV-2-infected hamsters treated with dexamethasone. N = 5 hamsters per group (controls as in panel d for reference). **(I)** Representative images (left) and quantification (right) of perivascular fibrosis in the Masson trichrome-stained lungs of infected hamsters treated with dexamethasone. N = 5 hamsters per group. **(J)** Representative images and **(K)** quantification of the heavily immune-infiltrated areas from hematoxylin and eosin-stained lungs of dexamethasone-treated hamsters infected with SARS-CoV-2 (controls as in Figure 4g for reference). N = 5 lungs per group. **(L)** Representative images (showing MPO signal in cyan) and **(M)** quantification of neutrophil infiltration to the lungs of SARS-CoV-2-infected golden hamsters treated with Dexamethasone (controls as in Figure 4d for reference). N = 30 random fields from 5 lungs per group. **(N)** Viral load quantification by real-time PCR from lungs of hamsters treated with vehicle (control), disulfiram (pre- and post-infection treatment groups) and dexamethasone. N = 6 hamsters (vehicle, disulfiram post-treatment and dexamethasone groups) and 5 hamsters (disulfiram pre-treatment group). **(O)** Weight loss curves of all groups, showing no differences between all groups. N = 6 hamsters per group. Bars show mean ± S.E.M, ***$P < 0.001$; n.s., not significant and p-values shown as determined by unpaired two-tailed Student's t-test analysis (D, E, F, H, I, K, M) or one-way ANOVA with Tukey's multiple comparison test (N).

Legends for supplemental videos:

- **Supplemental Video 1: NETs are abundant in the lungs of TRALI-induced mice treated with vehicle.** Representative whole mount tissue clearing of lungs from vehicle-treated mice subject to TRALI, and stained for the vasculature (CD31, grey), DNA (DAPI, blue), neutrophils (MPO, cyan) and citrullinated histone 3 (citH3, red).

- **Supplemental Video 2: NETs are scarce in the lungs of TRALI-induced mice treated with disulfiram.** Representative whole mount tissue clearing of lungs from Disulfiram-treated mice subject to TRALI, and stained for the vasculature (CD31, grey), DNA (DAPI, blue), neutrophils (MPO, cyan) and citrullinated histone 3 (citH3, red).

- **Supplemental Video 3: Disulfiram-treatment reduces edema formation in the lungs of mice subject to TRALI.** 3D reconstructions of CT scans showing the bone, lung and edema volumes in mice treated with Disulfiram or vehicle, at baseline (before TRALI induction) and 21 minutes after TRALI induction.

- **Supplemental Video 4: NETs are abundant in the lungs of SARS-CoV-2-infected golden hamsters treated with vehicle.** Representative whole mount tissue clearing of lungs from vehicle-treated golden hamsters infected with SARS-CoV-2, 6 days post-infection, and stained for the DNA (DAPI, blue), neutrophils (MPO, cyan) and citrullinated histone 3 (citH3, red). Autofluorescence is shown in gray for reference.

- **Supplemental Video 5: NETs are scarce in the lungs of SARS-CoV-2-infected golden hamsters treated with disulfiram.** Representative whole mount tissue clearing of lungs from Disulfiram-treated golden hamsters infected with SARS-CoV-2, 6 days post-infection, and stained for the DNA (DAPI, blue), neutrophils (MPO, cyan) and citrullinated histone 3 (citH3, red). Autofluorescence is shown in gray for reference.

Legends for supplemental tables

- **Supplemental Table 1:** Differential expression analysis of the RNA-seq dataset comparing disulfiram- vs. vehicle-treated lungs (treated 24 h prior to infection) from SARS-CoV-2-infected hamsters.

- **Supplemental Table 2:** GO terms (biological processes) of the differentially expressed genes comparing disulfiram- vs. vehicle-treated lungs from SARS-CoV-2-infected hamsters.

- **Supplemental Table 3:** Reactome pathway analysis of the genes downregulated in response to disulfiram in SARS-CoV-2-infected hamsters.

- **Supplemental Table 4:** Clustering of the Reactome pathway analysis of the genes downregulated in response to disulfiram in SARS-CoV-2-infected hamsters.

- **Supplemental Table 5:** Clustering of the Reactome pathway analysis of the genes upregulated in response to disulfiram in SARS-CoV-2-infected hamsters.

- **Supplemental Table 6:** Differential expression analysis of the RNA-seq dataset comparing disulfiram- vs. vehicle-treated lungs (treatment started one day after infection) from SARS-CoV-2-infected hamsters.

- **Supplemental Table 7:** Reactome pathway analysis of the differentially expressed genes comparing disulfiram- vs. vehicle-treated lungs (treatment started one day after infection) from SARS-CoV-2-infected hamsters.

- **Supplemental Table 8:** GO terms (biological processes) of the genes downregulated in response to disulfiram (treated one day after infection) in SARS-CoV-2-infected hamsters.

- **Supplemental Table 9:** Common GO terms on both treated 24 h prior to infection and treated one day after infection lung RNA-seq datasets (defined as not significantly different).